Analysis of the Post-Stimulation Functional Magnetic Resonance Imaging Signal Undershoot

Kamakshi Advani, B. Eng.

Department of Biomedical Engineering
Faculty of Medicine
McGill University, Montreal, QC, Canada

A thesis submitted to the Faculty of Graduate Studies and Research in partial fulfillment of the requirements of the degree of Master of Engineering.

Your file Votre référence
ISBN: 978-0-494-32576-6
Our file Notre référence
ISBN: 978-0-494-32576-6

Abstract

The blood oxygenation level dependent (BOLD) functional magnetic resonance imaging (fMRI) signal, the most commonly used imaging technique to identify localized changes in brain activity, has been shown to exhibit certain transient characteristics that are poorly understood by the medical imaging community. This thesis is aimed at investigating the origins of the post-stimulation signal undershoot phenomenon, a prolonged (~30s-1min) drop below baseline of the BOLD signal after the cessation of neuronal stimulation.

Three alternate theories exist regarding the physiological changes responsible for the BOLD undershooting. The first theory suggests that prolonged elevation in the cerebral metabolic rate of oxygen ($CMRO_2$) is responsible for the undershooting in the BOLD time course. The second theory, referred to as the 'Balloon model', suggested that prolonged dilation of the post-capillary blood vessels, causing an accumulation of paramagnetic deoxygenated blood, results in the post-stimulus BOLD signal dipping below pre-stimulation levels. Yet another theory suggest that the BOLD signal mimics changes in the cerebral blood flow (CBF) time course, which has been shown, in some studies, to exhibit post-stimulus undershooting.

Two fMRI experiments were performed on separate groups of healthy human volunteers. The first experiment involved measuring BOLD and CBF changes during a single level of visual and motor stimulation as well as two levels of mild (5 and 10% CO_2) hypercapnia. During the second experiment, BOLD and CBF signals were measured under visual and motor stimulation of variable duration. In both experiments, the BOLD and CBF data were analyzed to determine a relationship between the post-stimulus behavior of BOLD and CBF time course and the corresponding stimulation/hypercapnia condition.

Results demonstrated clear post-stimulus BOLD and CBF undershoots during hypercapnia as well as neuronal activation, strongly suggesting that elevated $CMRO_2$ levels can be ruled out as the sole cause of the undershooting. Other scenarios, including the Balloon model prediction and the undershooting observed in the CBF signal time-course, as possible contributors to the BOLD post-stimulus undershooting are discussed.

Resumé

L'effet BOLD (blood oxygenation level dependent) est la technique de l'imagerie a résonance magnétique fonctionnelle la plus répandue. Cette technique, qui est utilisée pour l'identification des changements locaux de l'activité cérébrale, contient certaines varations temporelles incomprises par la communauté d'imagerie médicale. Le but de cette dissertation est d'étudier les origines d'une diminution prolongée (~30s-1min) du signal BOLD en dessous du niveau de base après la fin de la stimulation neuronale, nommé le undershoot post-stimulus.

Trois théories existent sur les changements physiologiques responsables du undershoot dans le signal BOLD. La première suggère que le undershoot est causé par une augmentation du niveau de consommation d'oxygène pendant une période prolongée. Le modèle ballon illustre qu'une dilatation prolongée des vaisseaux sanguins post-capillaires (venules?) cause une accumulation du sang déoxygéné paramagnétique, provoquant une chute du signal BOLD en-dessous du niveau de pré-stimulation. La troisième théorie suggère que le signal BOLD suit les changements du flux sanguin cérébral (CBF), qui est lui-meme caracterisé par un undershoot post-stimulus.

Pour cette dissertation, deux expériences d'IRMf ont été menées sur des groupes d'humains volontaires et en santé. La première expérience consistait d'un acquisition des

signaux BOLD et CBF pour un seul niveau de stimulation visuelle et motrice ainsi que deux niveaux légers d'hypercapnies (5 et 10 %). Pour la deuxième, les signaux BOLD et CBF on été mesurés sous stimulations visuelles et motrices de durées variables. L'ensemble des données des deux expériences a été analisé pour déterminer la relation entre le comportement post-stimulus des décours temporels du BOLD et CBF et la condition correspondante de stimulation/hypercapnie.

Les résultats démontrent des undershoots post-stimulus dans les signaux BOLD et CBF suite a l'hypercapnie ainsi que les activations neuronales. Ces resultats suggèrent que le niveau surélevé de CMRO2 n'est pas la seule cause du undershoot. D'autres facteurs sont proposés comme contributeurs potentiels au undershoot post-stimulus du BOLD. Entre autres, la prédiction du modèle ballon et les undershoots observés dans le décours temporel du signal CBF sont considérés.

Acknowledgements

First and foremost I'd like to thank Dr. G. Bruce Pike, who guided me though this master's thesis and made my graduate school experience a very enjoyable one. I'm also very grateful to Jean Chen, for her support, late of hours spent acquiring and deciphering image and endless patience in editing my written work. With fond memories of cookies, beer, and server problems, I'd like to acknowledge my fellow lab mates, Bojana, Jan, Mark-ette, Leili, Mike, Ives, Jen, Charmaine, Ilana, Vivian, E-Kat, Clarisse, Christine, and Mallar, who made the lab a great place to work. Jennifer and Andre, for ensuring that the practical things were under control. Ron, Dave and Louise, for help (and candy) at the scanner. Finally I'd like to thank Sardar for his patience and support through this entire experience.

Table of Contents

List of figures

List of tables

Glossary of terms

ADP	adenosine diphosphate
ANOVA	analysis of variance
ATP	adenosine triphosphate
ASL	arterial spin labeling
BASSI	bandwidth-modulated adiabatic selective saturation and inversion
BOLD	blood oxygenation level dependent
CBF	cerebral blood flow
CBV	cerebral blood volume
CMR_{glu}	cerebral metabolic rate of glucose
$CMRO_2$	cerebral metabolic rate of oxygen
CNR	contrast-to-noise ratio
CPMG	Carr-Purcell-Meiboom-Gill
CSF	cerebrospinal fluid
dHb	deoxyhemoglobin
EDRF	endothelial-derived relaxing factor
EEG	electroencephalography
EPI	echo planar imaging
EPISTAR	echo-planar imaging and signal targeting with alternating radio frequency
$ETCO_2$	end-tidal CO_2
FAIR	flow-sensitive alternating inversion recovery
fMRI	functional magnetic resonance imaging

fNIRS	functional near-infrared spectroscopy
FOV	field of view
FWHM	full-width-at-half-maximum
GABA	gamma-aminobutyric acid
GRE	gradient echo
GTP	guanosine triphosphate
Hb	hemoglobin
HRF	hemodynamic response function
MC	motor cortex
MION	monocrystalline iron oxide nanocolloid
MR	magnetic resonance
MRI	magnetic resonance imaging
MNI	Montreal Neurological Institute
OEF	oxygen extraction function
oHb	oxyhemoglobin
$PaCO_2$	partial pressure of CO_2 in blood
pO_2	arterial pressure of oxygen in blood
PASL	pulsed arterial spin labeling
PET	positron emission tomography
PICORE	proximal inversion with control for off-resonance effects
QUIPSS	quantitative imaging of perfusion using a single subtraction
RF	radio frequency
ROI	region of interest
SE	spin echo
SNR	signal-to-noise ratio
T_1	spin-lattice relaxation constant
T_2	spin-spin relaxation constant
TE	echo time
TI	inversion time
TR	repetition time
VASO	vascular space occupancy

VC	visual cortex
vCBV	venous cerebral blood volume
VERVE	venous refocusing for volume estimation
Y	blood oxygen saturation

Piled Higher and Deeper ***by Jorge Cham*** **www.phdcomics.com**

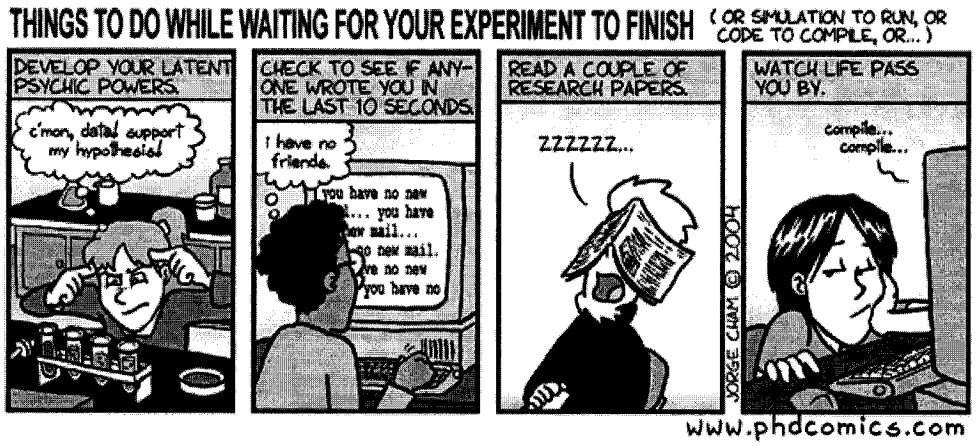

title: "Things to do..." - originally published 2/6/2004

Chapter 1

Introduction

For over a century, neuroscientists have been in pursuit of a thorough understanding of how the brain functions, requiring the mapping of brain activity and an understanding of the processing taking place during the activity. Typically, following the electrochemical process that results in neuronal firing, an increase in metabolism is observed, along with enhanced blood flow to the activated area which supplies metabolites and removes metabolic by-products. Over the years, several imaging tools such as positron emission tomography (PET), electroencephalography (EEG) and functional magnetic resonance imaging (fMRI) have evolved to detect neuronal activity, by exploiting metabolic, electro-chemical and hemodynamic changes that accompany activation. These techniques have been invaluable in the study of normal brain function as well as in assessing various neurological disorders (e.g. stroke, tumors and epilepsy).

Functional Magnetic Resonance Imaging (fMRI), an interdisciplinary field involving neuroscientists, physicists and clinicians, has been rapidly growing both as a research tool and for clinical purposes due to its versatility, flexibility and simplicity as compared with other brain imaging techniques. FMRI attempts to localize neuronal activity by measuring signal fluctuations caused by hemodynamic and metabolic changes

immediately following the activity. Although several fMRI techniques exist, the Blood Oxygenation Level Dependent (BOLD) method has gained immense popularity since its introduction in 1990 [1, 2]. BOLD fMRI makes use of the fact that when activity increases in a region of the brain, the local magnetic resonance (MR) signal increases by a small amount due to changes in blood oxygenation. Today, BOLD-fMRI is used as the principle non-invasive technique to map patterns of activation in the human brain.

Despite its widespread use for over a decade, our understanding of the precise physiological changes that give rise to the BOLD phenomenon remains incomplete. Numerous sources of evidence have led to the understanding that the BOLD signal increases during activity due to the dilution of deoxyhemoglobin (dHb) in the venous vessel, dHb being a paramagnetic by-product of aerobic metabolism that reduces the MR signal. The excess blood flowing into the vessels, in response to the increased metabolic activity, causes the dilution. Considerable research has been dedicated to deciphering the quantitative relationship between neuronal activity and the resultant BOLD signal via the modeling of cerebral metabolic rate of oxygen consumption ($CMRO_2$), cerebral blood flow (CBF), cerebral blood volume (CBV), and geometric changes in cerebral vasculature in response to brain activity.

In addition to steady state behavior, the BOLD signal time course exhibits several transient features at the onset and offset of neuronal activity, which suggest a complex transient uncoupling between the various physiological parameters. A concrete theory explaining the occurrence of the transients will no doubt shed invaluable light on the physiological origin of the BOLD signal. Recently, two alternate models have been proposed to explain the transient post-stimulus undershooting observed in the BOLD signal time course. The 'balloon model' [3, 4] predicts distensible venous vessels at the

root of the post-stimulation undershoot, while the sustained elevated $CMRO_2$ theory [5, 6] suggests that elevated oxygen consumption after the cessation of the neuronal response as the source of the BOLD undershoot. Further, some researchers believe that a post-stimulus decrease in blood flow may also play some part in causing the BOLD undershoot [7, 8]. To date, there is a paucity of studies to verify either one of the theories.

In this thesis, two complementary experiments are performed to test the validity of the two theories for the undershooting phenomenon mentioned above. In the first experiment, functional BOLD and CBF data are acquired from healthy human subjects under normocapnia visual/motor stimulation and hypercapnia conditions. The presence and the nature of the BOLD post-stimulus undershoot in the hypercapnia data are investigated to substantiate the theories regarding the origins of the undershoot. In the second experiment, BOLD and CBF data acquired from healthy human subjects during visual and motor stimulation of varied duration are used to investigate the response of the BOLD undershoot to changes in stimulation duration. Significant increases in undershoot duration with stimulation duration would provide support for the elevated $CMRO_2$ theory.

The present thesis consists of seven chapters. Chapter 2 provides an overview of brain physiology, including the hemodynamics that accompany neuronal activity. Chapter 3 describes the fMRI techniques, namely BOLD and arterial spin labeling (ASL), which are most commonly used to detect blood oxygenation and blood flow changes respectively. A description of the BOLD signal transients and the proposed theories regarding their origins are also introduced. Chapter 4 details the two experiments performed to test the two currently prevalent theories for the BOLD signal post-stimulus undershoot. The corresponding results are presented in chapter 5 and 6 respectively, and discussed in chapter 7. The thesis is concluded with a discussion of future work.

Chapter 2

Brain Physiology

2.1 Neuronal Physiology

2.1.1 Basic structure and function of a neuron

The nervous system is made up of the brain, the spinal cord and a complex interconnection of peripheral neurons. Using a universal pattern of frequency and temporally encoded electrical signals, the nerve cells communicate with one another in performing various sensory, motor and cognitive functions. Although neurons come in a variety of shapes and sizes, their characteristic structure can be described in terms of a cell body or soma with multiple tree-like extensions called dendrites and a single long axon (*c.f.* Figure 2.1). The role of the dendrites is to receive incoming electrical signals from other neurons; the soma is responsible for cell metabolism and protein synthesis, while the axon is concerned with generating and propagating the electrical impulses. The axon ends in a synapse where the electrical signal is transmitted to the pre-synaptic terminals of adjacent neurons via an electrochemical process involving neurotransmitters and ion exchange.

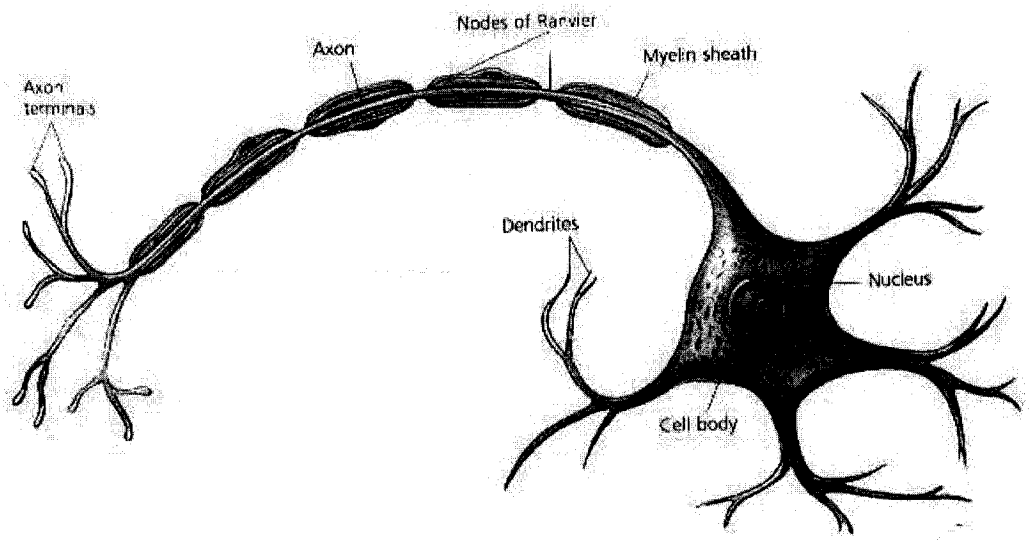

Figure 2.1: Basic structure of a neuron (adapted from [9]).

Electrical signals are generated and propagated through the neuron via a complex mechanism of electrochemical changes (a thorough explanation of neuronal signal processing can be found in [10]). Under equilibrium conditions the intracellular space of the nerve cell has a net negative charge, typically –60 to –70 mV, compared with the extracellular space. This imbalance in charge is known as the 'resting membrane potential' and is determined by the concentration gradients and the relative permeability of potassium [K^+] and sodium [Na^+] ions across the cell membrane. At rest the concentration of K^+ is higher within the cell and the concentration of Na^+ is higher outside (K^+=95 mM and Na^+=30 mM inside whereas K^+=3 mM and Na^+=120 mM outside [10]). A K^+ concentration gradient towards the outside of the cell causes the K^+ ions to flow out of the cell membrane (the cell membrane being freely permeable to K^+ ions but restrictive to the inflow of Na^+ ions). An active sodium-potassium pump, using adenosine triphosphate (ATP) hydrolysis to provide energy, maintains the K^+ and Na^+ gradients despite the flow of ions across the membrane: 3 Na^+ ions are expelled for each 2 K^+ ions

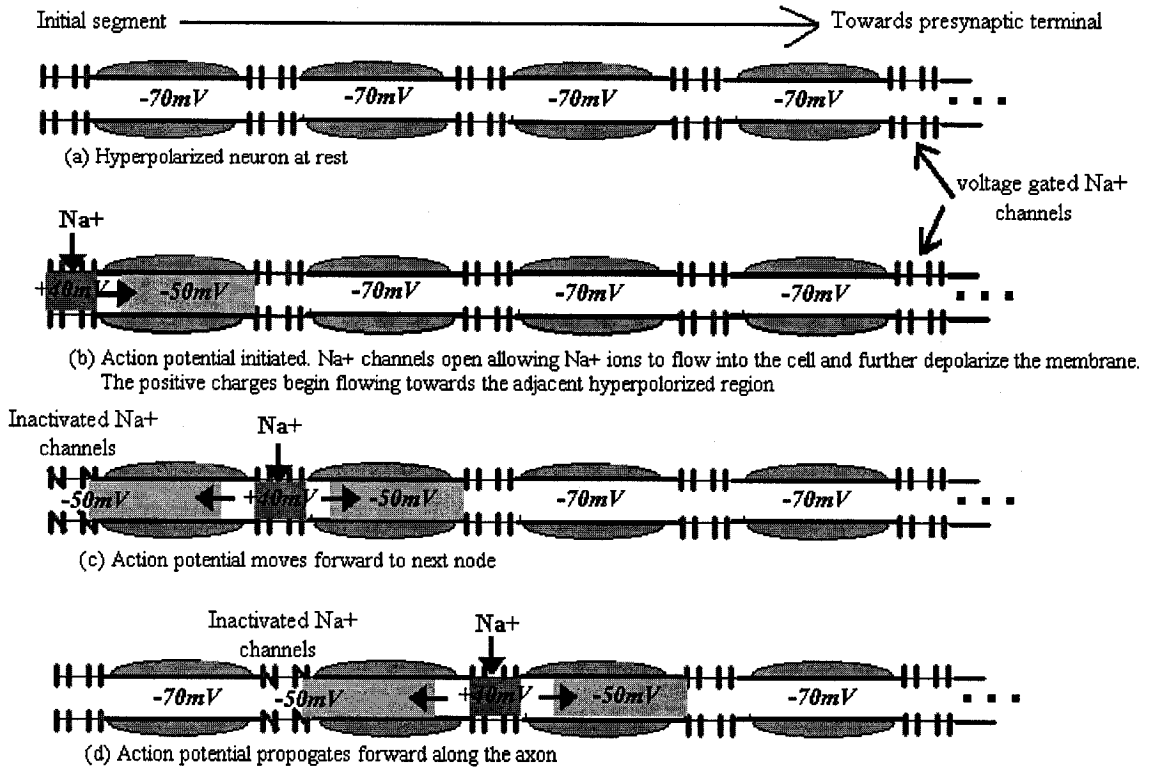

Figure 2.2: Action potential propagation from the initial segment to the pre-synaptic terminal of a single neuron.

actively forced into the cell using 1 molecule of ATP [10].

During brain function neurons fire, sending electrical signals down the axon. Information is propagated along the axon by means of a rapid, brief depolarization of the axon membrane from the resting membrane potential of about -70 mV to +40 mV, referred to as the 'action potential' (*c.f.* Figure 2.2). The passive propagation of the action potential is maintained along the length of the axon by regularly placed voltage-gated sodium channels on the membrane surface. At resting membrane potential, the voltage-gated sodium channels remain closed. As the action potential moves along the membrane, thus depolarizing it, the channels open to allow the Na^+ ions to flow into the cell and cause further depolarization. Within a few milliseconds following depolarization (1-2 ms

[10]), the Na^+ ion channels inactivate themselves, stopping the influx of Na^+ ions. The action potential passes to the next segment further down the axon as the currently depolarized portion of the axon returns to the resting membrane potential.

The action potential propagates to the end of the axon where it is transmitted to the post-synaptic terminal of one or more adjacent neurons (typically the dendrites or the soma) (*c.f.* Figure 2.3). The pre-synaptic terminal contains synaptic vesicles filled with chemical neurotransmitter molecules (most common neurotransmitters include glutamate, glycine and gamma-aminobutyric acid (GABA)). The active zone of the pre-synaptic terminal is embedded with voltage gated calcium [Ca^{2+}] channels. When the action potential invades the pre-synaptic terminal, the Ca^{2+} channels open, resulting in a Ca^{2+} ion influx into the terminal. The Ca^{2+} ions react with the vesicles, causing them to fuse with the pre-synaptic membrane, which results in the release of neurotransmitter molecules into the synaptic cleft. The neurotransmitter molecules rapidly diffuse across the narrow synaptic cleft (typically 10 to 20 nm [10]) towards the post-synaptic terminals of the adjacent neurons. The post-synaptic terminal can be either an excitatory or an inhibitory terminal depending on the class of ion channels present. Excitatory synapses contain ligand gated Na^+ channels triggered by glutamate or glycine, while inhibitory synapses contain ligand gated Cl^- channels triggered by GABA. The neurotransmitter molecules bind with their respective ion channel receptors causing the channel to open and resulting in an influx of Na^+ or Cl^- ions into the post-synaptic region and a depolarization or a hyperpolorization of the post-synaptic neuron respectively. Thus, an excitatory synapse brings a neuron closer to the action potential threshold, while an inhibitory response makes it less likely for the post-synaptic neuron to fire an action potential. Generally, a single neuron almost simultaneously receives excitatory or inhibitory synapses from

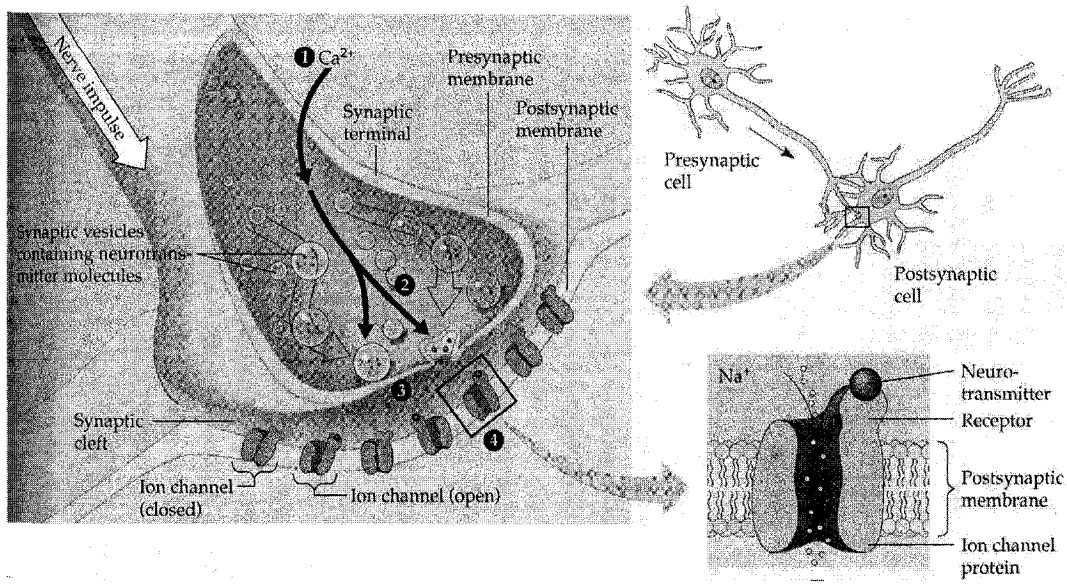

Figure 2.3: Synaptic terminal (adapted from [11]). Propagation of the nerve impulse from the per-synaptic terminal to the post-synaptic neuron.

several neurons, which accumulate additively to sufficiently depolarize or polarize the membrane, resulting in or preventing the initiation of an action potential.

Once the electrical impulse has been transmitted to the next neuron, the synaptic terminal returns to its resting condition; the synaptic ion gradients are restored via active transport and neurotransmitter molecules are regenerated and packaged into vesicles.

2.1.2 Glial cells

The central nervous system has another important class of cells called glial cells or neuroglia that provides structural and metabolic support to the neurons. One class of glial cells, called the astroglia, help in restoring the ionic gradients and in clearing the neurotransmitters from around synapses (*c.f.* Figure 2.4). The foot-processes of these cells wrap around the endothelial walls of the capillaries, providing a passageway for metabolic substrates and oxygen to reach the neuron and assist in the return of metabolic byproducts into the blood stream while preventing toxins from entering the brain.

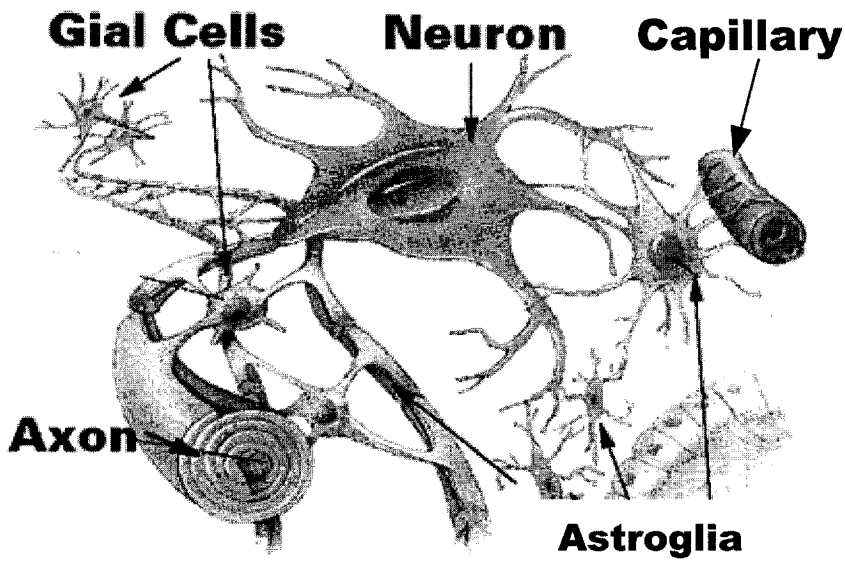

Figure 2.4: Glial cells(adapted from [11]). Astroglia provide a pathway for the transport of metabolic substrates and byproducts between blood capillaries and the neuron cell body.

This class of glial cells is an essential element in the study of brain metabolic function as they not only assist in the metabolic pathway but also consume significant amounts of energy in removing and recycling the unused neurotransmitter molecules from the synaptic cleft. Some studies suggest that approximately 80-90% of total cortical glucose metabolism occurs to support the glutamate/glutamine neurotransmitter cycle [12, 13] in the astrocytes.

2.2 Vascular Physiology and Hemodynamics

Although the brain weighs only 2-3% of total body weight, it receives about 15% of the total arterial blood output of the heart [10]. Blood, carrying metabolic substrates and oxygen, is brought to the brain via the vertebral and the internal carotid arteries. The internal carotid artery bifurcates to form the anterior and middle cerebral arteries, which deliver blood to the forebrain region. The anterior cerebral artery branches to supply the

cortex and penetrates the basal surface to supply deeper structures such as the basal ganglia, thalamus and the internal capsule. The middle cerebral artery supplies the temporal lobe, the anteriolateral frontal lobe and the parietal lobe. The two vertebral arteries unite to form the midline basilar artery, which further bifurcates into the posterior cerebral arteries, supplying the posterior cortex, the midbrain and the brainstem. The basilar artery joins the two internal carotid arteries to form a ring, called the Circle of Willis, at the base of the brain. This ring allows blood to shunt from one side of the brain to the other, assuring continuous blood supply to both sides of the brain (safeguarding against blockages in either one of the lateral arteries).

The drainage of the deoxygenated blood together with metabolic by-products from brain tissue is done via groups of deep and superficial veins. The deeper veins drain the choroid plexus, periventricular regions, diencephalon, basal ganglia and the deep white matter before draining into the cerebral veins. The superficial veins drain the cortex and the subcortical white matter before emptying into the sagittal and basal sinuses.

Although diverse in structure and function, all blood vessels are surrounded by a smooth, single-celled layer of endothelium. These cells serve as a permeability barrier for the exchange of nutrients and metabolic by-products to and from the tissue. Due to the presence of different amounts of smooth muscle and elastic tissue along the cell wall, the pressure in the vascular system decreases gradually from the arteries and arterioles to the capillaries, venules and finally the veins (*c.f.* Figure 2.5). The aorta and the large arteries contain large quantities of elastin in their epithelium and serve as low-resistance "pressure reservoirs" that stretch during a systole and contract during a diastole to propel blood

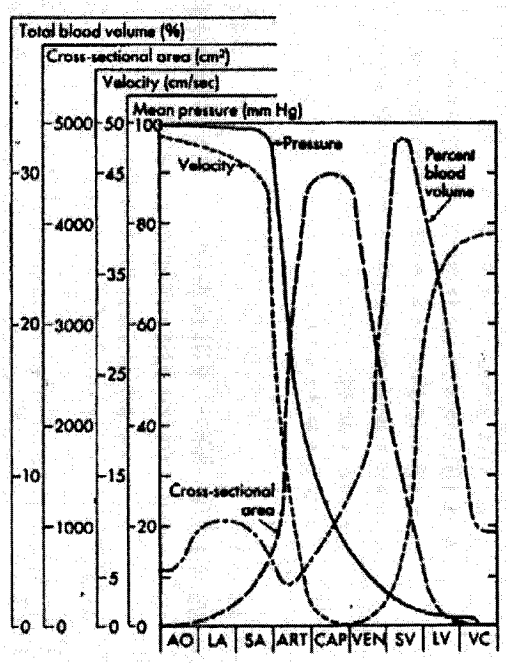

Figure 2.5: Changes in hemodynamic parameters across the vascular tree (adapted from [14]). AO: aorta; LA: large artery; SA: small artery; ART: arterioles; CAP: capillaries; VEN: venules; SV: small veins; VC: venae cavae.

towards target tissue (alternating in pressure between 120-80 mmHg [10]). Smaller arterioles act as resistive vessels due to their narrow size and the smooth muscle fibers present in their cell wall. These muscle fibers restrict their vascular compliance to changes in pressure caused by the alternating pulmonary systole and diastole mechanism. This ensures smooth and continuous blood flow to the tissue.

Apart from the normal flow pressure, smooth muscles in the arterioles regulate blood flow via vasodilatation or vasoconstriction of the vessel in response to metabolic, hormonal and neuronal signals. Hyperemia, a state of increased blood flow due to arteriolar dilation, is observed with increased brain activation or muscular activity. The spontaneous activation of the arterioles is triggered either by potassium ions (which

accumulate after repeated membrane depolarization during neuronal activation) or metabolic by-products like carbon dioxide, lactic acid and adenosine.

The arterioles branch into the capillaries, which are a few microns in diameter (inner diameter ~5 μm [10]) and are the sites where the majority of the nutrient and by-product exchange takes place. The capillary walls contain very little elastin and smooth muscle fiber. The endothelial wall in the capillaries consists of very tight cellular junctions that form the "blood-brain barrier". The foot-like processes of the astrocytic glial cells wrap around the capillary walls, forming a bridge to transport metabolic substrates and by-products between the endothelial wall of the capillaries and the cell soma of the neurons. The capillary membrane has a very high surface area to volume ratio and is permeable to water, carbon dioxide, oxygen, and some lipid soluble substances, partially permeable to small ions, and impermeable to plasma protein and non-lipid soluble molecules.

The capillaries unite to form venules and eventually veins. The endothelial walls of the veins, which are very thin and contain little elastin, are about 8 times more distensible than arteries [15]. Veins can accommodate large volumes of blood in response to small changes in internal pressure. They are known as the "volume stores" of the circulation (approximately 60% of blood volume is present in the systemic veins under resting conditions [10], while the arteries carry only ~30% and the capillaries ~5% [16,17]). When hyperemia occurs in response to neuronal activation, the veins respond to increased internal flow pressure by stretching their wall, thus resulting in increased venous cerebral blood volume. The walls of the veins are controlled by sympathetic nerves, which activate the smooth muscles in the cell wall causing a decrease in diameter and compliance of the vessel.

2.3 Metabolism and neuronal activation

The human brain consumes about 20% of the oxygen and 25% of the glucose needed by the body [18, 19]. Apart from the normal synthesis and repair of cells, the unusually high metabolic demand can be attributed to the energy intensive electrical and chemical changes that occur during neuronal activation, maintaining the membrane ion gradients (active transport of Na^+ and K^+ ions via the ATPase pump), and the release, reabsorption and regeneration (glutamate/glutamine cycle) of neurotransmitters around synapses. Most of the metabolic activity occurs in the outer gray matter of the cortex, which has the highest density of neurons and synaptic terminals in the brain [20, 21].

Under normal conditions the brain's energy demand is met by the break down of glucose molecules to produce adenosine triphosphate (ATP). Three distinct yet linked metabolic pathways are responsible for metabolizing glucose molecules: glycolysis, the Krebs cycle, and oxidative phosphorylation (a thorough explanation of the entire metabolic process can be found in [22]).

The initial step, known as glycolysis, is anaerobic and takes place in the cytosol of the metabolizing cell. Via several enzymatic steps, glucose is broken down into pyruvate and water, giving two ATP molecules, as described in Eq. 2.1.

$$C_6H_{12}O_6 + 2NAD^+ + 2ADP + 2Pi \rightarrow 2CH_3(C=O)COO^- + 2NADH + 2H^+ + 2ATP + 2H_2O \qquad (2.1)$$

The end product of the above reaction, pyruvate, can either enter the Krebs cycle or be converted into lactate, depending on the availability of oxygen. In the absence of oxygen, pyruvate is converted to lactate via a single, enzyme mediated reaction described in Eq. 2.2.

$$CH_3(C=O)COO^- + NADH + H^+ \rightarrow CH_3 - CHOH - COO^- + NAD^+ \quad (2.2)$$

Thus, the overall reaction of anaerobic glycolysis is given in Eq. 2.3.

$$Glucose + 2ADP + 2Pi \rightarrow 2Lactate + 2ATP + 2H_2O \quad (2.3)$$

Although energetically less efficient than the oxidation of glucose (described below), anaerobic glycolysis provides the fastest metabolic pathway and is characterized by the production of lactate in the tissue.

The Krebs cycle and oxidative phosphorylation together form the slower yet energetically much more prolific stage of glucose metabolism. In the second pathway, the aerobic Krebs cycle, small fuel fragments are broken down to give hydrogen atoms, CO_2, and small amounts of energy. Pyruvate from glycolysis, which is transported into the mitochondria of the cell and oxidized to acetyl coenzyme A (acetyl-CoA) and CO_2, serves as the primary molecule entering the Krebs cycle. Via a number of steps, guanosine triphosphate (GTP) is produced, the hydrolysis of which, like ATP, provides energy for some reactions. The overall equation for the Krebs cycle is given in Eq. 2.4. The energy from GTP can also be used in converting ADP molecules to ATP molecules.

$$Acetyl - CoA + 3NAD^+ + FAD + GDP + Pi + 2H_2O \rightarrow$$
$$2CO_2 + CoA + 3NADH + 3H^+ + FADH_2 + GTP \quad (2.4)$$

The hydrogen atoms formed in this stage (most of which are transferred to coenzymes NAD^+ and FAD to form NADH and $FADH_2$) are essential elements in the third oxidative phosphorylation pathway.

Oxidative phosphorylation is quantitatively the most important mechanism by which fuel molecules are transferred to ATP. Hydrogen atoms (either H^+ from NADH or

$FADH_2$) combine with oxygen to release energy, which is transferred to ATP. The phosphorylation reaction is given in Eq. 2.5.

$$\frac{1}{2}O_2 + NADH + H^+ \rightarrow H_2O + NAD^+ + Energy \tag{2.5}$$

Overall, the amount of energy released by the catabolism of glucose to CO_2 and water is about 686 kcal/mol of glucose [10]. The net reaction of the aerobic catabolism of glucose in the brain is described in Eq. 2.6.

$$C_6H_{12}O_6 + 6O_2 + 36ADP + 36Pi \rightarrow 6CO_2 + 6H_2O + 36ATP \tag{2.6}$$

The rate of the above process is limited by the availability of glucose, oxygen and ADP. In doing cellular work, ATP molecules undergo hydrolysis to ADP and an inorganic phosphate group (Pi). An increase in the concentration of ADP (as compared with ATP) suggests a shortage of energy within the cell, thus initiating ATP production by upregulating glucose metabolism.

During neuronal activity increases, the neurons and glial cells utilize increased amounts of energy to restore ion gradients and neurotransmitter concentration. Thus, it follows that the brain's metabolic demand would increase during brain activation. Several researchers have studied the close coupling between the changes in the brain's metabolic demand and neuronal activity. The rate of glucose metabolism and oxygen consumption has been shown to rise and fall with focal neuronal activity [23, 24, 25].

Glucose and oxygen are delivered to the glial cells and the neurons by blood. Under resting conditions only about 50% of the glucose present in the blood is extracted and undergoes catabolism to release energy for brain function [26], the rest is cleared out through the veins. During neuronal activation the cerebral metabolic rate of glucose

(CMR_{glu}) increases to satisfy the elevated metabolic demand. The cerebral metabolic rate of oxygen ($CMRO_2$) also increases to a smaller degree [27]. Since there is a very limited buffer of oxygen in the blood and the extraction of oxygen from the blood is not very efficient, cerebral blood flow (CBF) increases to satisfy the elevated demand for oxygen during faster metabolism [28, 29].

Although the above explanation for metabolism-driven hemodynamic changes seems intuitive, Fox et al. in [18] reported a focal physiological uncoupling between the $CMRO_2$ and CBF changes during neuronal activation. PET results showed somatosensory stimulus induced focal increases in $CMRO_2$ (of about 5%) to be conspicuously smaller than CBF increases (of about 30%), suggesting that the homodynamic regulatory mechanism may be independent of metabolite build up or substrate depletion [18, 20].

Several scientists, including Magistritti et al. [12], Fox et al. [27] and Shulman et al. [30] have hypothesized that the increases in CBF, which correspond well with the higher glucose demand during activation [27], occur to support an alternate fast, non-oxidative glycolysis pathway, providing rapid energy for astrocyte-mediated neurotransmitter clearing during neuronal activation. Observations of focally elevated lactate levels in tissue during activation support this hypothesis [31, 32].

Buxton el al. proposed an alternate explanation for the CBF-$CMRO_2$ mismatch, suggesting that the two parameters are indeed tightly related via the 'oxygen limitation model' [28, 29]. The model suggests that under the assumption of efficient oxygen metabolism and no capillary recruitment, the oxygen extraction fraction decreases as flow velocity increases. Thus, large changes in flow are needed to support small increases in $CMRO_2$. Further, fMRI studies by Hoge et al. [33], using simultaneous blood flow and oxygenation level measurements (in an interleaved fashion) acquired during visual

stimulation, indicate a linear, approximately 2:1 flow-oxygen consumption coupling. Results showed that the linear relationship between blood flow and oxygen consumption was not stimulus dependent. Hoge's study supports the diffusion-gradient limitation on oxygen delivery theory [29].

Recent studies, focused on deciphering cerebrovascular coupling in the brain, have challenged many of the above metabolic pathway theories [34, 35], which suggests that vasodilatation is a consequence of increased energy demand. Attwell and Iadecola [36] suggest that the hemodynamic response is signaled by neurotransmitter release during neuronal firing. It is rather difficult to provide conclusive evidence for either mechanism because all the underlying changes co-vary closely during neuronal activity. Results from our lab [37] that examined the blood flow response to activation during globally increased resting flow showed that the incremental flow changes were approximately independent of resting flow levels, thereby favoring the direct signaling pathway suggested by Atwell et al [36].

2.4 Summary of physiological changes during neuronal activity

Neuronal activation is characterized by the creation and propagation of an action potential down the axon of the neuron, which is eventually transmitted to the adjacent neurons at the synaptic terminal. The ability of a neuron to fire and transmit the action potential to other neurons is dependent on the existence of an electrochemical ion gradient across the cell membrane of the neuron. The K^+ and Na^+ ion concentration gradients are maintained by the active transport of these ions against their concentration gradients using energy provided by the hydrolysis of ATP molecules. Thus, increased brain activity results in an

elevated metabolic demand (to provide energy to restore the continuous depletion of the ion gradients). The surge in glucose and oxygen demand (increases in $CMRO_2$ and CMR_{glu}) is met by increase in tissue perfusion (CBF) resulting from dilation of the arterioles feeding the tissue. The increased blood pressure is passed on to the veins, which swell to accommodate the increase in blood volume coming from the capillaries. As a result, we expect a delayed passive swelling of the veins and increased venous cerebral blood volume during neuronal activation.

In the next chapter, we present non-invasive MR imaging techniques to detect and measure blood oxygenation and blood flow changes in the brain.

Chapter 3

Functional Magnetic Resonance Imaging

Functional MRI (fMRI) is a non-invasive medical imaging technique used to identify subtle signal changes accompanying neuronal activity in response to stimuli tasks or physiological manipulation. FMRI techniques exploit variations in the MR signal, resulting from hemodynamic, physiological and metabolic changes coupled to neuronal activity, to localize the origin of the activity.

In a typical fMRI experiment, a time series of images is collected under different stimulation conditions. Corrected changes in the MR signal contrast (generally T_1, T_2 or T_2^*) between varying physiological conditions are used to reveal the location of the brain's response to the stimulus [38]. In this chapter, the two most common fMRI techniques, namely blood oxygenation level dependent (BOLD) fMRI, sensitive to changes in the concentration of deoxyhemoglobin [39], and the arterial spin labeling (ASL) techniques, used to measure perfusion [40, 41], are reviewed.

3.1 BOLD fMRI: measuring susceptibility changes during neuronal activity

As discussed in the previous chapter, neuronal activity is accompanied by a focal increase in metabolism and an increased delivery of metabolic substrates via up regulation of blood flow. About 98% of oxygen transport from the lungs occurs via the hemoglobin (Hb) molecules present within red blood cells, the remaining 2% of oxygen is directly dissolved in plasma [10]. Hemoglobin, an iron containing metalloprotein molecule present within red blood cells, consists of four globular protein sub-units, 2 □ and 2 □ peptide chains, non-covalently bound together. In each of the sub-units is embedded a heme group containing one Fe^{2+} ion, held in place by a histidine nitrogen bond. Each iron ion is capable of binding one oxygen molecule. Depending on the partial pressure of oxygen in the plasma, one Hb molecule can therefore reversibly bind up to four oxygen molecules, resulting in an oxyhemoglobin (oHb) molecule. Under normal arterial pressure, pO_2 of 100mmHg, 1L of blood can transport the equivalent of up to 200ml of pure gaseous oxygen [10]. A fully oxygenated Hb molecule is diamagnetic, causing little or no distortions to the magnetic field in surrounding tissue.

The oxygen diffusion gradient, from red blood cells to tissue, causes the oxygen molecules to detach from the oxyhemoglobin molecule and diffuse into the adjacent tissue. These results in the formation of deoxyhemoglobin (dHb) in venous blood, with as many as four unpaired electrons per molecule of Hb. Due to the presence of the unpaired electrons, dHb exhibits paramagnetism that induces a non-zero magnetic field in the presence of (and aligned with) an external magnetic field. This induced magnetic field is seen as a local microscopic magnetic field inhomogeneity by the precessing hydrogen nuclei, leading to accelerated observed transverse relaxation and a reduction in the local

T_2 and T_2^* MR signal. Thus, paramagnetic dHb, a by-product of oxidative metabolism, serves as an endogenous contrast agent for gradient echo (T_2^*) and spin echo (T_2) MRI imaging.

The ratio of oxyhemoglobin concentration to total hemoglobin (the sum of oxy- and deoxyhemoglobin) concentration in blood is referred to as 'blood oxygen saturation' (Y). Under baseline conditions both cerebral blood flow (CBF) and the cerebral metabolic rate of oxygen ($CMRO_2$) are related so as to produce an average oxygen saturation level of ~98% in arterial blood, ~80% in capillary blood and ~60% in venous blood [42]. During neuronal activation, there is an increase in $CMRO_2$ and CBF. However, the increase in CBF exceeds the increase in $CMRO_2$ [20, 29, 33]; the relationship between neuronal activity and the two parameters is poorly understood. Although the $CMRO_2$ increase acts to decrease the Y level, the disproportional increase in CBF produces a net increase in blood oxygenation in the capillaries and veins. Capillary and venous oxygenation levels rise by ~6% and ~12% respectively [42] during typical activations. The resultant elevation in venous-blood oxygenation level (or a net dilution of the total paramagnetic dHb present in the tissue) causes the local MRI signal to intensify [2]. Thus, each period of brain activation is accompanied by a focal increase in the MR signal.

To summarize, the local microscopic inhomogeneities in the magnetic field caused by magnetic susceptibility difference between oxygenated and deoxygenated hemoglobin produce a signal difference that is used as a measure of focal activity. BOLD fMRI data is obtained using gradient echo T_2^* weighted imaging or spin echo T_2 weighted imaging; in observing the signal difference between images obtained during and in the absence of focal brain activation. The BOLD signal difference is widely accepted as an indicator of neuronal activity. However, its precise quantitative interpretation is yet to be

fully deciphered [3, 43, 44] (discussed in detail below). Other fMRI techniques like perfusion-based MRI methods are used to provide additional information regarding brain hemodynamics and metabolism.

3.2 Arterial Spin Labeling: measuring blood perfusion

Perfusion refers to the delivery of arterial blood (carrying oxygen and nutrients) to tissue via the microvascular capillary network. An assessment of CBF, or the rate of delivery of arterial blood to a local brain voxel, has applications in managing disorders such as stroke and Alzheimer's disease as well as in understanding normal brain physiology. Two main classes of fMRI methods are used to measure blood perfusion: the intravascular contrast agent method (also used for cerebral blood volume (CBV) measurements), and the arterial spin labeling (ASL) technique. ASL, an MRI technique using magnetically labeled blood water as an endogenous contrast agent, has advantages over traditional tracer-based MRI and PET techniques due its non-invasiveness, repeatability and higher signal-to-noise ratio (SNR).

CBF measurements using ASL are obtained by acquiring, in an interleaved manner, MRI images of two alternating states: control and tagged images. The control images are obtained without magnetically altering the blood spins. Quantitatively, fully relaxed arterial blood in the control image carries an intrinsic magnetization M_{0B}. In the tagged images, blood spins proximal to the imaging slice(s) are typically inverted using a 180-degree RF inversion pulse applied in a plane through the major feeding artery. The magnetically labeled blood water that flows into each tissue element in the imaging slice(s) is proportional to the CBF. On arrival at the imaging slice, the longitudinal magnetization (M_z) of the tagged blood which perfuses the surrounding tissue is

measured. The blood in the tagged image ideally (ignoring relaxation between tagging and imaging) carries $-M_{0B}$ magnetization. The amount of blood delivered to the tissue within the time interval TI_2 (time between the180-degree inversion pulse and the image acquisition) is $f \times TI_1$, where f is the local CBF and TI_1 is the time width of the tagged bolus. Subtracting each adjacent pair of control and tag images results in the entire static tissue signal being removed, leaving a signal proportional to the labeled blood flow. Thus, the difference image is a function of CBF as shown in Eq. 3.1:

$$\Delta M \propto 2M_{0B}.f.TI_1 \tag{3.1}$$

The change in the net magnetization, ΔM, is usually only ~1% compared to M_{0B} [40]. The SNR of the resulting difference images are generally low and need to be averaged to produce accurate CBF maps.

Since its inception in the early 1990's [45, 46], the ASL technique has grown in application, being used to quantify steady-state CBF and activation induced changes in CBF. Based on how the tagging is done, several variations of the technique exist, for example EPISTAR [47], FAIR [48], PICORE [49], QUIPSS [50] and QUIPSS II [51]. Most of these techniques suffer from systemic errors caused by two related vascular effects. First, the imaged CBF signal is sensitive to the transit delay (□t) between the application of the tag and the arrival of the tagged blood into the imaging slices. Second, it may include signal from intravascular tagged blood destined to perfuse more distal regions in the brain. Both issues arise due to the fact that the time required for the tagged blood to reach the imaging region is similar to the T_1 decay time constant of blood, making it necessary to acquire images simultaneously with various dynamic effects like blood delivery, exchange, clearance of the tag by flow and T_1 decay. If the image is

acquired too soon after the application of the tag (at $t<<\delta t$), the CBF measurement may be underestimated due to the presence of the transient delay, or overestimated (if $t=\delta t$) due to the tagged intravascular signal traveling through the imaging slices. If the image is acquired too long after the tagging (at $t>>\delta t+\tau$, where □is the time width of the tag), the tagged signal is attenuated due to T_1 decay. The amount of tagged magnetization entering the imaging slice(s) and therefore the ASL difference signal varies linearly with time as shown in Eq. 3.2:

$$\Delta M = \begin{cases} 0 & t < \delta t \\ 2M_{0B} f (t-\delta t) e^{-t/T_{1B}} q(T_{1B}, T_{1T}, T_{ex}, f, \lambda, t) & \delta t < t < \delta t + \tau \\ 2M_{0B} f \tau e^{-t/T_{1B}} q(T_{1B}, T_{1T}, T_{ex}, f, \lambda, t) & \delta t + \tau < t \end{cases} \quad (3.2)$$

where M_{0B} is the relaxed magnetization of arterial blood, f is the CBF in units of mL-blood/mL-tissue/min, T_{1B} is the T_1 of arterial blood, T_{1t} is the T_1 of brain parenchyma, T_{ex} is the transit time from the distil edge of the tag region to the capillary bed where the tagged blood water exchanged with the brain parenchyma, □is the blood-brain partition coefficient of water, and q is the correction factor for the exchange of tag water from blood to tissue (safely approximated to 1).

The QUIPSS II technique, developed by Wong et al. [51] tries to overcome the above systemic errors by making the measurements insensitive to variations in the transit delay (*c.f.* Figure 3.1). At time TI_1 after the application of the tag (usually between 600-700ms [51]), a saturation pulse is applied to the tagging region to cut off the tail end of the inflowing tag. Thus, the time width (□) of the delivered tagged blood is precisely TI_1. The inclusion of the tagged intravascular signal is reduced by a relative long TI_2 (between 1200-1400ms [51]), to allow the intravascular signal to flow out before the perfused tagged-blood is imaged. The increased TI_2, although responsible for increased T_1 decay of

the tag, has little effect on quantifying CBF. In this manner, the QUIPSS II method makes it possible to obtain robust CBF measurements insensitive to transit delay and, by creating a well-defined tailing end of the bolus tagged blood in conjunction with a long TI_2, allows for the clearance of intravascular tag before image acquisition. The QUIPSS II ASL difference signal, independent of δt and τ, is given in Eq. 3.3:

$$\Delta M = 2M_{0B} f TI_1 e^{-TI_2/T_{1B}} q(T_{1B}, T_{1T}, T_{ex}, f, \lambda, t) \tag{3.3}$$

Although the BOLD technique, due to its simplicity and ability to produce images with relatively high contrast-to-noise ratio (CNR), remains the standard for activation related mapping of the brain, several questions still exist regarding the origin and localization of the BOLD signal [3, 43, 44]. As a result, the ASL technique has become an important tool to investigate the hemodynamic changes underlying BOLD fMRI. In this thesis, I use the QUIPSS II ASL technique to better understand the physiological origins of activation correlated BOLD signal changes.

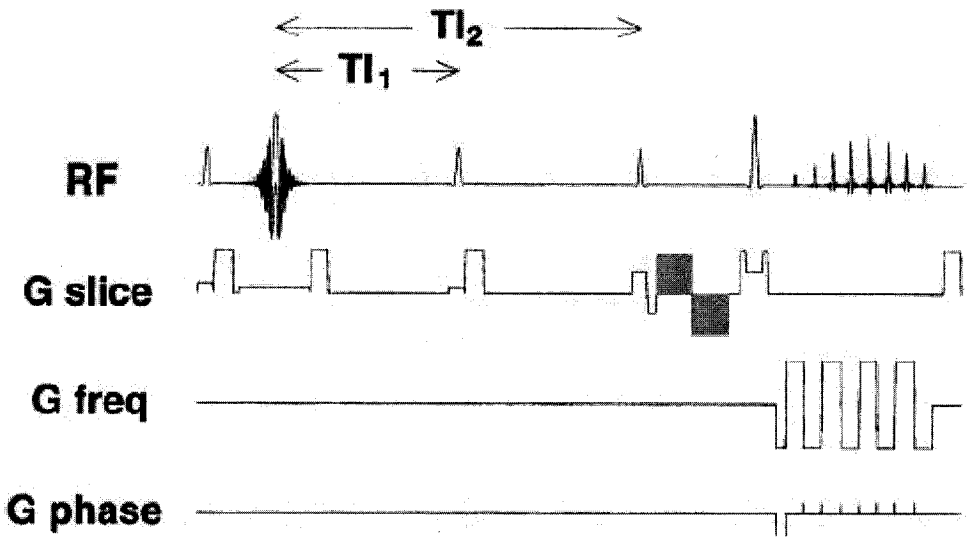

Figure 3.1: Pulse sequence for ASL (adapted from [51]). RF pulse from left to right: (1) in plane pre-saturation to null spins in the imaging slice; (2) inversion tag; (3) QUIPSS II saturation to end tagging; (4) 90° excitation pulse; (5) 180° refocusing pulse; (6) readout.

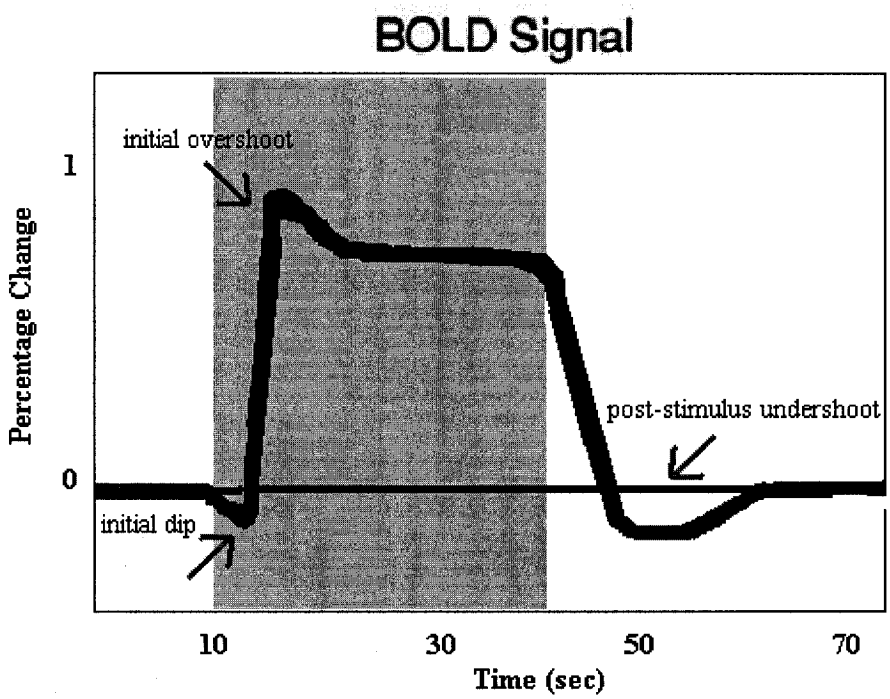

Figure 3.2: Typical BOLD response. The activation block is indicated by the gray region. The three BOLD signal transients: initial dip, initial overshoot and the post-stimulus undershoot are shown.

3. 3 Understanding the BOLD signal transients

BOLD fMRI is a very powerful noninvasive tool to investigate the functioning of the brain during neuronal stimulation. Although it has been used in several thousand functional brain mapping studies over the past two decades [2, 52, 53, 54, 55, 56, 57, 58], some ambiguity still remains about the mechanism underlying the BOLD signal. The transient relationship and the temporal response characteristics of the underlying CBF, CBV, $CMRO_2$ and vessel geometry are subjects of ongoing investigation.

An interesting phenomenon in the BOLD time-course is the transient behavior observed at the onset and the offset of the stimulus (*c.f.* Figure 3.2). A brief negative initial dip (~1-3s) [59, 60, 61, 62], followed by a large positive post-onset overshoot [3, 63, 64] is often observed on presenting a step function stimulus. The BOLD signal then attenuates over 6-10s to a plateau level [3]. Finally, on cessation of the stimulus (i.e. step down), a prolonged negative undershoot lasting ~ 30s-1min is often observed [3, 7, 63, 64, 65]. An intense interest in the BOLD transients has risen over the past decade; a better understanding of these transients will provide invaluable insight into the origins of the BOLD response and help in the design and interpretation of fMRI experiments.

A short (~2-3s) initial dip has been reported in MR spectroscopy [59, 66], optical imaging [60, 61] and a few MR [60, 67] studies. This phenomenon, which is believed to be highly localized to the site of activation [68], is thought to occur due to an initial increase in deoxyhemoglobin caused by elevated $CMRO_2$ before the vasculature has time to up-regulate the CBF. Although this explanation remains largely undisputed, most BOLD fMRI studies fail to report any observations of the initial undershoot [3, 62, 63, 64]. The failure to observe this transient is often attributed either to the low temporal

resolution of BOLD fMRI as compared to optical imaging techniques, the low sensitivity of BOLD experimental analysis towards small negative signals, or to the relatively poor spatial localization of the BOLD signal. The measured BOLD signal arises not only for microvasculature sites of activation, but also from the draining veins distal from the area of activation. This effect is undesirable as it makes the BOLD signal localization less accurate.

The initial overshoot that follows is thought to be the result of a coarse upregulation in the CBF in response to activation, followed by its gradual fine tuning, reflected in the decline of the BOLD signal to its steady-state plateau level [3, 64]. Studies that show similar transient overshoot behavior in the CBF time-course support this hypothesis [7, 64].

The BOLD post-stimulus undershoot is the most pronounced transient. The cessation of the stimulus causes a normalization of CBF, while a still elevated venous dHb level causes the BOLD signal to drop below baseline before it slowly recovers to pre-stimulation intensity levels. Two alternate theories have been proposed to explain the prolonged increase in venous dHb concentration: the Buxton balloon model [3, 4], and the elevated $CMRO_2$ model [5, 6].

Several groups including Buxton et al. [3, 4, 8], Mandeville et al. [69, 70] and Stefanovic et al. [71] advocate the theory that the distensible venous vessels continue to remain in the 'ballooned' state for several seconds after the cessation of the stimulus and the CBF's return to baseline. Although oxygen extraction returns to baseline, the increased total dHb in the 'ballooned' veins, no longer diluted by the excess CBF, is responsible for the BOLD undershoot.

Further, some MRI [7, 72], Doppler ultrasound [73] and laser Doppler flowmetry [74] studies have documented similar (although less pronounced) undershoot behavior in the CBF time-course, while other perfusion MRI studies describe the CBF signal as returning smoothly to pre-stimulus baseline levels without demonstrating any undershoot [3, 64, 70, 75]. The observation of an undershooting CBF signal has prompted groups including Hoge et al. [7] and Friston et al. [76] to suggest that, in addition to the venous ballooning, the BOLD undershoot is driven by similar trends in the post-stimulus CBF signal.

Others groups, like Frahm et al. [5, 6], Lu et al. [72] and Schroeter et al. [77], suggest that the BOLD signal undershoot occurs due to increased dHb concentration caused by sustained elevated $CMRO_2$ levels after the CBF has returned to baseline. They propose that a prolonged increase in energy demand, satisfied by elevated oxidative metabolism, is needed in doing work to restore ion gradients and replenish tissue oxygen stores that were depleted during neuronal activation [78].

In order to better explain and quantify the BOLD fMRI signal, several mathematical models have been developed. These models have the ability to quantitatively estimate BOLD signal changes resulting from variations in underlying hemodynamic parameters.

3.4 Modeling of the BOLD fMRI signal

Several mathematical models have been proposed to provide a link between basic hemodynamic and metabolic changes and the resultant BOLD signal response. An integrated model, which includes influential elements from Ogawa's work [79], Grubb's

power law relationship [80], Buxton's Balloon model [3], Mandeville's Windkessel model [70], and work by Davis [81] and Hoge [43], to name a few, is described in this section (a more complete description of the same can be found in [8, 39]).

3.4.1 BOLD signal model

The BOLD signal arises due to physiological changes during brain activity that result in changes in local dHb concentration. Relative changes in CBF and $CMRO_2$ determine the level of oxygenation in the blood while changes in CBV determine the total amount of blood in the voxel. The physical process that gives rise to the MR signal has been thoroughly studied by Boxerman [82, 83], Ogawa [79], Weisskoff [84], and Yablonsky and Haacke [85]. The simplest model for the gradient echo MR signal is given in Eq. 3.4.

$$S = S_{\max} \cdot e^{-TE \cdot R_2^*} \qquad (3.4)$$
$$R_2^* = R_2^*(0) + R_{dHb}$$

where TE stands for echo time and S_{max} is that MR signal that would be measured at TE=0. The transverse relaxation rate constant R_2^* is the sum of two components: $R_2^*(0)$, which represents the relaxation rate in the absence of dHb, and R_{dHb}, the additional relaxation produced by the presence of dHb in the blood. Note that the $R_2^*(0)$ term is much larger than the R_{dHb} term, that is, the local T_2^* is dependent on the intrinsic T_2 of the tissue and the gradient field through the voxel, and the effect of the dHb is relatively small, thus resulting in a small but measurable activation related BOLD signal change. Assuming that R_{dHb} is the only parameter that changes during activation, the baseline normalized BOLD signal change with activation, $\Delta S = S_{act} - S_0$ is:

$$\frac{\Delta S}{S_0} = e^{-\Delta R_2^* . TE} - 1 \approx -\Delta R_2^* . TE \tag{3.5}$$

$$\Delta R_2^* = R_{act} - R_0$$

To determine the role of dHb in changing the MR signal intensity, it is necessary to model the dependence of R_2* changes on oxygen extraction and blood volume. A reasonable approximation for the relationship between relaxation rate and dHb content as given by Davis et al. [81] is:

$$R \propto VE^{\beta} \tag{3.6}$$

where $\beta = 1.5$ is a good empirical approximation for 1.5 - 3T fields [79, 82, 83, 85]. The value of β being greater then 1 suggests that the transverse relaxation depends not only on total dHb content in the voxel but on other complex effects like diffusion taking place at the capillary level and the signal change of the blood itself.

Following the ideas described above, a model for activation induced BOLD signal changes in terms of oxygen extraction and blood volume can be written as:

$$\frac{\Delta S}{S_0} \approx A \cdot \left[1 - \frac{V_{act}}{V_0} \left(\frac{E_{act}}{E_0} \right)^{\beta} \right] \tag{3.7}$$

where A is a lumped parameter that includes TE and the proportionality constant from Eq. 3.6. The changes in the BOLD signal depend on the resting blood volume V_0 and resting oxygen extraction E_0. A decrease in either V or E will result in the decrease in the total dHb concentration and thus an increase in the BOLD signal. Parameter A represents the ceiling effect or the maximal BOLD signal increase that could occur corresponding to a complete removal of dHb from all blood compartments.

In attempting to relate the physiological changes in $CMRO_2$ and CBF during neuronal activation to the BOLD signal, we know that brain activity triggers changes in

arterial resistance leading to an increase in focal CBF. As the arterial resistance decreases, the pressure in the capillaries and the veins causes an increase in vessel volume or CBV. Grubb et al. [80] experimentally derived the power law to describe the relationship between steady-state CBF and CBV changes:

$$v = f^{\alpha} \tag{3.8}$$

where v and f represent the baseline normalized CBV and CBF parameters respectively and the approximate value of the exponent α = 0.4. This relationship applies to entire blood volume.

Further, $CMRO_2$ can be written in terms of net oxygen extraction fraction (E), arterial oxygen concentration (C_a) and CBF.

$$\begin{aligned} CMRO_2 &= E \cdot C_a \cdot CBF \\ m &= \frac{E}{E_0} f \end{aligned} \tag{3.9}$$

where m represents the baseline-normalized value of $CMRO_2$. Eq. 3.8 and 3.9 represent the relationship between the key physiological parameters that change to produce the BOLD signal contrast.

Using the notation from Eq. 3.8 and 3.9, Eq. 3.7 can be written in terms of local physiological parameters as follows:

$$\frac{\Delta S}{S_0} = A \cdot \left(1 - f^{\alpha-\beta} m^{\beta}\right) \tag{3.10}$$

The model described above is useful to calibrate BOLD studies [43, 81] due to its explicit use of the CBF parameter f, which can be measured independently using ASL MRI. Further, $CMRO_2$ changes can be estimated by acquiring BOLD and CBF data and performing the appropriate data analysis [81]. However, this model is a steady state

model; it fails to account for the BOLD signal transients that occur at the onset and the offset of the stimulation block.

3.4.2 Buxton's Balloon model

To model the transients in the BOLD signal, the 'balloon model' [3] was proposed. This model provides an integral link between the various dynamic physiological parameters and the measured BOLD response. It is capable of generating BOLD time courses and transients that match experimental data [3, 8, 86, 87, 88]. The model suggests that the venous component of the blood vessel acts as an expandable balloon, whose volume is determined by the pressure difference between the inflow and outflow of blood into the venous vessel. The inflow rate of blood ($f_{in}(t)$) is equal to CBF, while the outflow rate of blood ($f_{out}(t)$) is a function of blood volume and pressure in the venous compartment. Using this model, the BOLD post-stimulus undershoot can be explained by a net increase in dHb present in the venous balloon, resulting from the slower return of CBV to baseline, as compared to CBF, at end of a stimulation block.

In order to quantitatively describe the balloon model, an alternate description for BOLD signal changes, written in terms of the BOLD signal's dependence on normalized blood volume, v, and normalized total deoxyhemoglobin, q, is used [8]:

$$\frac{\Delta S}{S} \approx V_0[a_1(1-q)-a_2(1-v)] \tag{3.11}$$

where V_0 is the resting blood volume fraction (typically 0.05) and a_1 and a_2 are dimensionless proportionality constants that depend on several experimental and physiological parameters. For a magnetic field of 1.5T with TE = 40ms and E_0=0.4, the constants were estimated to be a_1 = 3.4, and a_2 = 1.0 [8]. The above equation is based on

the assumption that the BOLD signal arises from small post-capillary venous vessels where the role of diffusion can be neglected. Thus, the signal changes depend entirely on the total amount of dHb present in the blood (first term in Eq. 3.11) and venous volume changes (second term in Eq. 3.11). Eq. 3.11 models the transient BOLD response while Eq.3.10 models the steady state BOLD signal changes.

The balloon model equations represent mass conversation of the two dynamic variables; total normalized dHb or q, and normalized venous CBV or v, passing through the venous balloon:

$$\frac{dq}{dt} = \frac{1}{\tau_{MTT}}\left[f(t)\frac{E(t)}{E_0} - \frac{q(t)}{v(t)} f_{out}(v,t) \right] \tag{3.12}$$

$$\frac{dv}{dt} = \frac{1}{\tau_{MTT}}\left[f(t) - f_{out}(v,t) \right] \tag{3.13}$$

Eq.3.12 represents the rate of change of total dHb as a function of net flow ($f_{in} - f_{out}$), scaled by oxygen extraction rate ($E(t)$) and vCBV. The resting value of oxygen extraction is typically $E_0 = 0.4$. The scaling time constant (τ_{MTT}) represents the mean transit time through the balloon at rest; typically $\tau_{MTT} = 2$s for a blood flow rate of 60ml min^{-1}/100ml of tissue and a resting venous blood volume of $V_0 = 0.02$. The quantity $f_{in}(t)E(t)$ is the driving function in the system. While $E(t)$ is an independent dynamic quantity, $f_{in}(t)E(t)/E_0$ represents the normalized cerebral metabolic rate of oxygen (normalized $CMRO_2$ or m). Eq.3.13 represents the rate of change of venous volume in the vessel as a function of net flow ($f_{in} - f_{out}$) scaled by the mean transit time constant.

To incorporate the vasoelastic effects of the distensible venous vessel, the outflow of blood, $f_{out}(t)$, is modeled as a function of balloon volume and the rate of change of the volume as follows:

$$f_{out}(v) = v^{\frac{1}{\alpha}} + \tau \frac{dv}{dt} \tag{3.14}$$

Eq.3.14 describes the initial resistance of the elastic venous vessels to volume changes followed by the ballooning, eventually settling in a steady state that conforms to the power law relationship expressed in Eq.3.8. The time constant □controls the duration of the transient changes; two different time constants, □ and □, reflect the inflatory and deflatory delays respectively. Non-zero values for □ are responsible for creating the post stimulus undershoot. Figure 3.3 shows the balloon model predictions for variations in each of the dynamic parameters responsible for the BOLD signal.

Although the balloon model remains largely undisputed, experimental validation of the model, by independently acquiring fMRI BOLD, CBF and venous CBV data, still remains to be done. Until recently, no non-invasive technique existed to measure venous CBV. Total CBV measurements have been obtained using monocrystalline iron oxide nanocompound (MION) contrast experiments, and were restricted to animal studies. With the recent development of non-invasive MRI techniques to quantify total CBV [89] and venous CBV (vCBV) [71], experimental validation of the balloon model may soon be possible. Moreover, the availability of such techniques could resolve the debate of the underlying physiological changes and the origin of the post-stimulus transients in the BOLD signal.

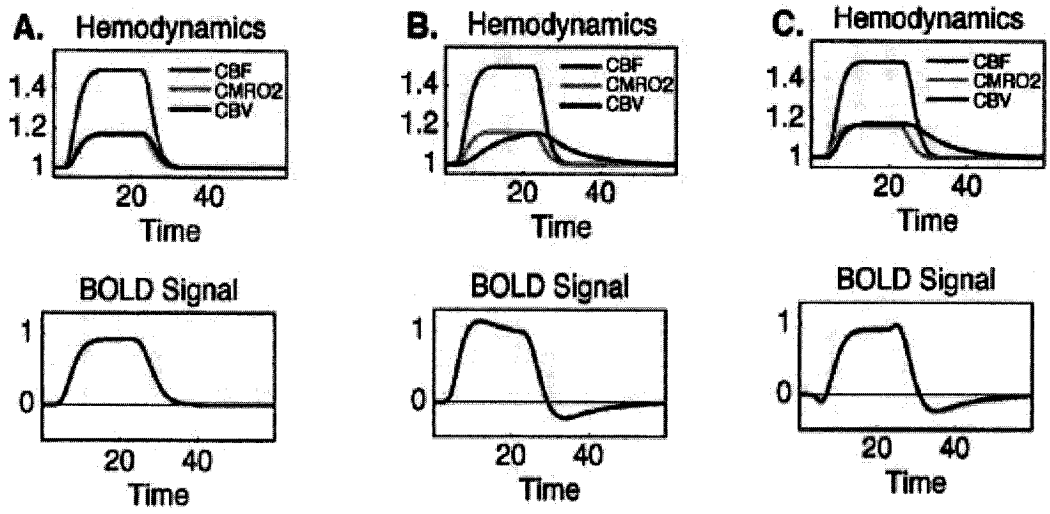

Figure 3.3: Transients in the BOLD response due to variations in the timing of the CBF, CBV and $CMRO_2$ responses (adapted from [4]). (A) shows a simple BOLD response, CBF, CBV and $CMRO_2$ parameters have similar time courses ($\tau_+ = \tau_- = 0s$); (B) BOLD response with initial overshoot and post-stimulus undershoot caused due to slow CBV response ($\tau_+ = \tau_- = 20s$); and (C) BOLD response with initial dip, created due to a small delay (~1s) in the CBF response.

3.5 CBV measurements

As discussed above, the BOLD signal arises due to the complex, still poorly understood, interplay between CBF, CBV and $CMRO_2$. Another potential problem associated with the BOLD fMRI method is that of spatial localization of the signal: BOLD activation maps, which are usually derived from statistical analysis of the image voxel CNR, are biased by the BOLD contrast signal arising from large veins that can be somewhat distal from the site of neuronal activity [89, 90]. Additionally, BOLD can only be used to detect activation related changes in total dHb relative to baseline levels, which serves as an indirect measure of brain activation. To overcome these problems and to help resolve the debate on the origins of the BOLD transients, new non-invasive MRI techniques have recently been developed to quantify total CBV [89] and venous CBV (vCBV) [71]. Measuring CBV permits direct investigation of the coupling between neuronal activity

and blood volume without including the complex interactions among the other parameters [90, 91].

The vascular space occupancy (VASO) technique recently described by Lu et al. [89] selectively nulls the vascular blood signal using a non-selective inversion pulse, before measuring changes in the tissue volume as the tissue water relocates to the blood component. A decrease in the VASO signal measured by the sequence is used to determine increases in microvascular CBV. Although this technique has been used in recent studies [89, 92, 93], some concerns about the perfect nulling of blood and contamination by the blood flow and cerebrospinal fluid (CSF) signal still remain. Moreover, this technique is designed to estimate total CBV changes rather than venous CBV changes which have been implicated in BOLD transient phenomenon.

Stefanovic et al. [71] introduced the venous refocusing for volume estimation (VERVE) technique. By exploiting the dependency of the R_2* of paramagnetic deoxygenated blood on the CPMG (Carr-Purcell-Meiboom-Gill) refocusing intervals, this method quantifies changes in vCBV. The venous blood signal is isolated by taking the difference between images obtained with short and long refocusing intervals. Although currently still at its infancy, this technique targets activation related venous CBV changes and would be invaluable in studying BOLD transients. The VERVE sequence, currently a single slice acquisition developed for 1.5T MR environment will have to undergo further development for multi-slice and higher field acquisition.

3.6 Summary

In this chapter, I discussed the most common functional MR imaging techniques, namely the BOLD and ASL technique used in mapping brain dHb and in measuring cerebral perfusion respectively. BOLD fMRI is the most popular MR technique which detects focal neuronal activation in the brain by exploiting changes in the T_2^* contrast that arise due to changes in dHb concentration. A change in dHb concentration level is a function of blood flow, oxygen extraction, blood volume and the biophysical properties of the blood vessels in the brain. Detailed biophysical models describing activation related BOLD signal changes in terms of the underlying physiological and hemodynamic changes were presented. The occurrence and the potential origin of the BOLD signal transients- namely the initial dip, the initial overshoot and the post-stimulus undershoot were discussed. The balloon model and the elevated $CMRO_2$ models, which provide alternate explanations for the BOLD signal post-stimulus undershoot were described. In the next chapter, I will describe experiments aimed at resolving which model best explains the post-stimulus undershoot. Using independent, interleaved BOLD and blood flow (QUIPSS II ASL) fMRI measures, I thus attempt to provide insight into the physiological changes underlying the post-stimulus undershoot transient.

Chapter 4

Theory and Methodology

As noted in the previous chapters, considerable debate exists around the origin of the BOLD signal post-stimulus undershoot. The 'balloon model' suggests that the undershoot occurs when the CBF signal returns to baseline soon after cessation of the stimulus while the venous CBV level remains elevated due to the elastic property of venous vessels [3]. The elevated venous CBV level thus causes an increase in the total paramagnetic deoxyhemoglobin present, resulting in a negative BOLD signal.

With the advent of non-invasive CBV fMRI techniques such as VASO [89] and VERVE [71], measurement of functional changes in CBV in humans has recently become more feasible. A recent study using VASO for CBV measurements suggests that the BOLD post-stimulus undershoot is better explained by continued elevation in post-stimulus $CMRO_2$ levels for up to 30 seconds [72], the increased oxygen consumption being used to restore synaptic ion gradients that were depleted during activation [78]. Functional near-infrared spectroscopy (fNIRS) studies seem to agree with this theory [77].

In this thesis, I study the transient post-stimulus undershoot phenomenon by performing interleaved BOLD and CBF experiments during visual and motor activation,

and under mild hypercapnia conditions. I hypothesize that, if the balloon model prediction is valid (i.e. the undershoot occurs due to the delayed return of the CBV signal to baseline levels after the end of the stimulus), a clear BOLD post-stimulus undershoot would be observed in both the visual/motor cortex activation and hypercapnia time courses. If, on the other hand, the elevated $CMRO_2$ after the cessation of the stimulus is responsible for the undershoot, an undershoot would be expected only in the visual/motor cortex activation data timecourse. In the case of the hypercapnia, there is no depletion of metabolites as the CBF levels are passively increased via inhalation of CO_2, thus no post-stimulus undershoot would be seen.

Additionally, through a second experiment, I investigate whether the amplitude and the duration of the post-stimulus undershoot is affected by the duration of the functional stimulus. If elevated $CMRO_2$ is responsible for the BOLD undershoot, I hypothesize that as the stimulation duration increases, the undershoot would last longer and be more pronounced, as $CMRO_2$ has to remain elevated for a period of time related to the stimulus to restore the ion gradient to its pre-stimulus concentration. Conversely, if the undershoot is caused by a passive change in the geometry of the venous as suggested by the balloon model, I expect the undershoot to be relatively independent of the stimulation duration.

4.1 Theory

4.1.1 Hypercapnia

Hypercapnia refers to the presence of abnormally high levels of carbon dioxide in circulating blood [94]. In functional MRI experiments, the hypercapnia condition is used

to up-regulate global CBF and is achieved in subjects by administering elevated levels of CO_2 (between 2-10% CO_2, with 21% O_2 and balance N_2) with medical air.

An increase in the CO_2 level in blood causes the perivascular pH level to decrease via a bicarbonate reaction. The diminished pH level causes the production of endothelial-derived relaxing factor/nitric oxide (EDRF/NO) in the vascular endothelial cells or the perivascular nerves [95], which alters the tone of cerebral vascular smooth muscles. The blood vessels dilate, resulting in a global increase in CBF. Although the complete mechanism by which CO_2 stimulates NO synthesis remains to be determined, there is clear evidence that the partial pressure of carbon dioxide ($PaCO_2$) is an important signal in modulating cerebral circulation through EDRF synthesis, while having no significant effect on the $CMRO_2$ [96]. In this study, several levels of CO_2 induced hypercapnia are used to modulate overall CBF levels in human subject.

4.1.2 BOLD fMRI sequence

As discussed in the previous chapter, the BOLD technique isolates brain activation by recording susceptibility differences between oxygenated and deoxygenated blood. The paramagnetic dHb produced during oxidative metabolism in the brain alters the transverse relaxation rate of blood ($T_{2(blood)}^*$). BOLD data is most commonly acquired using T_2^*-weighted gradient-echo echo planar imaging (EPI) sequences (*c.f.* Figure 4.1), which capture activation related changes in the $T_{2(blood)}^*$ over time.

The typical 2-D BOLD sequence uses a selective excitation pulse followed by a gradient echo EPI readout. A gradient echo image, formed by the application of a dephasing gradient followed by a rephasing gradient of equal amplitude, isolates T_2^*

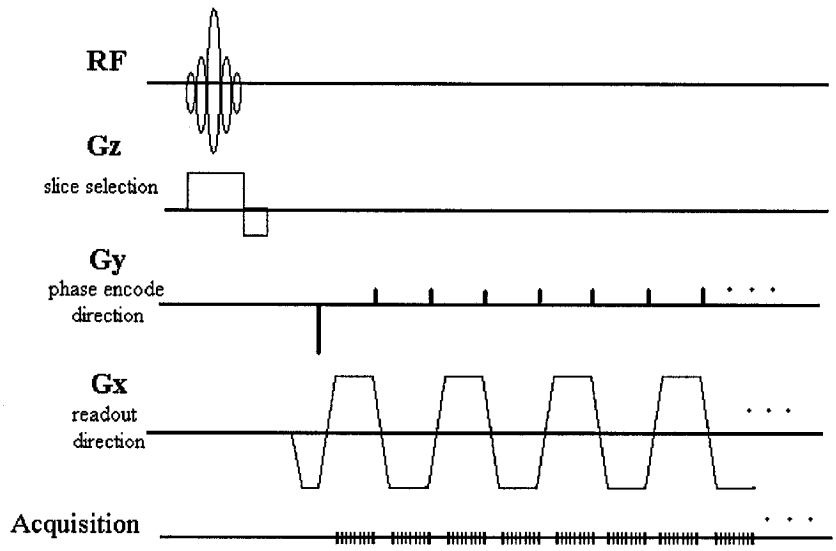

Figure 4.1: The gradient echo EPI sequence used in BOLD acquisition.

relaxation. The EPI train produces a series of gradient echoes with a bipolar oscillating readout gradient before the transverse magnetization decays away due to T_2^* relaxation.

Each gradient echo line in the EPI train is individually phase-encoded, (the phase-encoding gradient in incremented for each k-space line), so that the entire image can be acquired with one RF excitation. Thus, the gradient echo EPI sequence provides an efficient MR imaging technique with the temporal resolution needed to track changes in the BOLD signal (typically ~50-100ms per slice).

4.1.3 QUIPSS II fMRI sequence

The QUIPSS II ASL technique is a robust way to measure baseline and activation related CBF. It has advantages over other ASL techniques like FAIR and EPISTAR due to its insensitivity to variations in the bolus transit delay. The QUIPSS II sequence is a

modified inversion recovery sequence (*c.f.* Figure 4.2) followed by either gradient echo (GRE) or spin echo (SE) EPI readout.

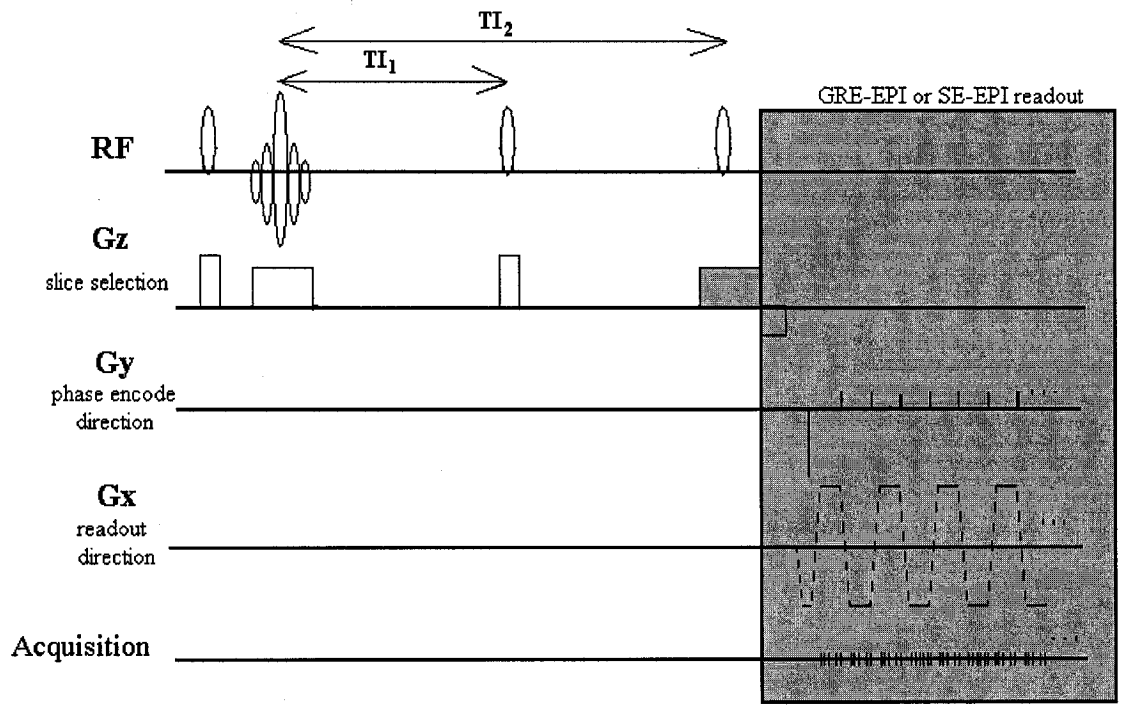

Figure 4.2: The QUIPSS II ASL sequence. RF pulses from left to right: (1) in-plane saturation pulse, (2) 180° selective inversion pulse, (3) saturation pulse to end tagging region, (4) 90° excitation pulse for EPI readout.

To begin, a slice selective saturating pulse (90° RF pulse) is applied to the imaging slices to increase the signal range and hence the contrast between inflowing blood and stationary tissue. A selective inversion tag (180° RF pulse), used to produce a labeled magnetization at the tagging location, immediately follows the initial saturation pulse. At time TI_1 after the inversion tag, a second saturation pulse is applied to end the tag and create a sharp cut-off. In the case of the control image the inversion tagging is not performed. The tagged blood flows into and perfuses the tissue in the imaging slice/s. At time TI_2 after the tagging, the image is acquired using a single shot EPI readout. The optimal values for the two time constants, TI_1 and TI_2, have been empirically found to be

between 600-700ms and 1200-1400ms respectively [51]. Subtracting temporally adjacent pairs of control and tag images results in the ASL difference signal, which is proportional to the perfusion in the imaged tissue.

In this study, the QUIPSS II technique was implemented with the GRE-EPI readout to acquire CBF data.

4.2 Methods

The main objectives of this study were 1) to investigate if the BOLD signal's post-stimulus undershoot is seen in the hypercapnia data time courses as well as in those of the visual and motor cortex activation data; and 2) to investigate whether the size and duration of the post-stimulus undershoot varies with visual and motor stimulation duration. In this section, details describing the experimental design, the MRI data acquisition and the data analysis used to meet these objectives are presented.

4.2.1 Experimental Design

4.2.1.1 Experiment #1: Investigating the occurrence of the BOLD post-stimulus undershoot in hypercapnia data

Two stimulus types were used for this experiment: A) sequential figure-to-thumb apposition (motor task) at ~3Hz frequency (cued by a metronome) while being presented with a radial flashing yellow/blue checkerboard contrast (visual stimulus), and B) two levels of hypercapnia (5% and 10% CO_2) at visual and motor baseline.

The visual stimuli were generated using locally developed GLStim software based on the OpenGL graphics library (Silicon Graphics, Mountain View, CA). The baseline condition consisted of a uniform gray field, while the activation pattern was a yellow-blue

radial checkerboard with 30 spokes and 3 rings of equal radial thickness, reversing contrast at 4Hz (*c.f.* Figure 4.3). Throughout the visual/motor stimulation experiment, the subjects were required to fixate on a small white arrow presented at the center of the field of view (FOV). The arrow randomly reversed direction from time to time (◂ or ▸). The stimulus was presented using an adjustable back-projection mirror mounted on the MR head coil.

The hypercapnia condition was induced by administering a mixture of CO_2 and air through a non-rebreathable facemask. (Hudson RCI, Model 1069, Temecula, CA). At baseline, the subjects inhaled medical air, supplied at 10L/min. During the hypercapniac perturbation, a prepared mixture of 10% CO_2, 21% O_2, and balance N_2 (BOC Canada Ltd. Montreal, Quebec) was combined with the medical air via a Y-connector. The CO_2 concentration was adjusted to 5% and 10% for the two experimental conditions, while maintaining the total flow rate of 10L/min. End-tidal CO_2 was measured via a nasal cannula using a monitoring aspirator (Normocap 200, Datex Inc., Plymouth, ME).

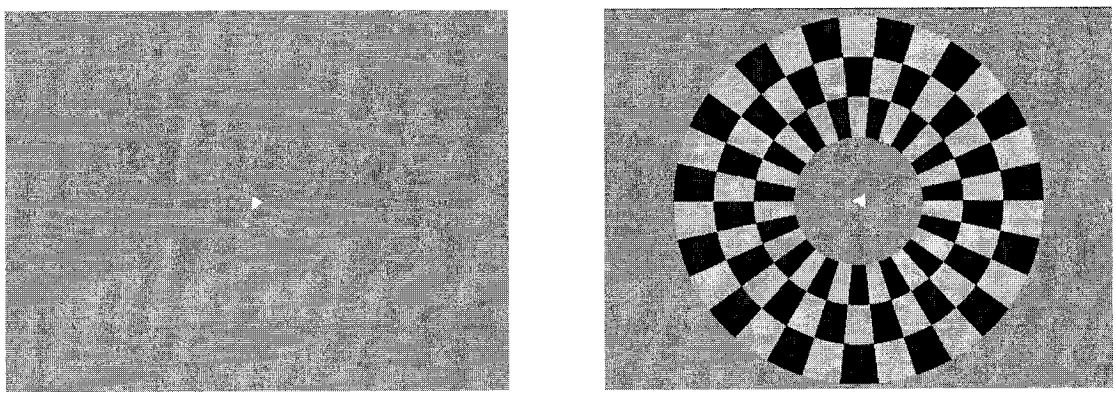

BASELINE ACTIVATION

Figure 4.3: Pattern used for visual stimulation. The baseline pattern comprised a simple uniform gray field. The activation pattern comprised a yellow-blue radial checkerboard pattern rotating at 4Hz. A small white arrow, randomly changing direction, was presented at the center of the screen to maintain the subject's attention.

Three functional runs, one for the combined motor and visual stimulation condition and one each for the two levels of hypercapnia, were performed on 11 healthy volunteers (4 male and 7 female, mean age 25.9 $\pm$ 3.4 years) in randomized order. Each run consisted of gray baseline, followed by three repetitions of 40s/80s/200s OFF/ON/OFF blocks (*c.f.* Figure 4.4). The 80s initial baseline condition was used to obtain an accurate normalization of the functional time course.

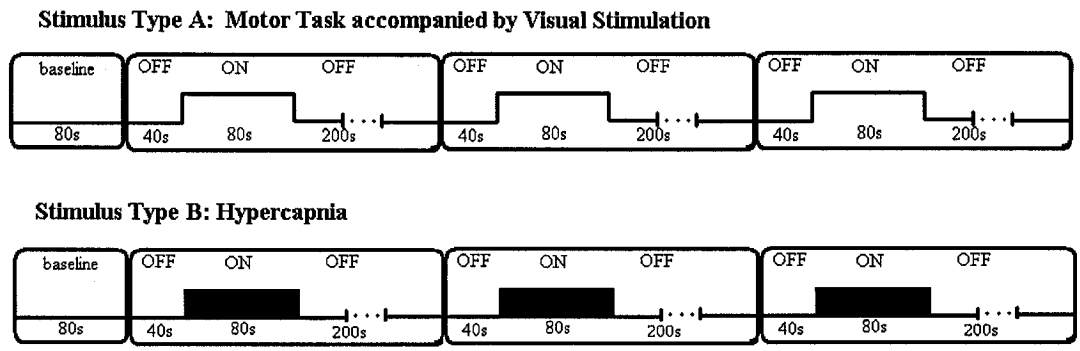

Figure 4.4: Design for Experiment #1. The functional experiment consisted of three runs, each comprising an 80s baseline and three 40s/80s/200s OFF/ON/OFF stimulation blocks. Stimulus type A was presented once while stimulus type B was performed twice, once each for 5% and 10% hypercapniac levels.

4.2.1.2 Experiment #2: Relationship between stimulation duration and BOLD post-stimulus undershoot

For this experiment, the stimulus consisted of sequential figure-to-thumb apposition (motor task) at ~3Hz frequency (cued by a metronome) while being presented with a radial flashing yellow/blue checkerboard contrast (visual stimulus). The visual stimulus was similar in nature and presentation to the one used in experiment #1.

Four functional runs were performed on 10 healthy volunteers (5 male and 5 female, mean age 26.2 $\pm$ 3.6 years). Each run consisted of an initial 80s baseline condition (used to normalize the time course) during which the subject rested and focused

on a uniform gray baseline followed by repetitions of OFF/ON/OFF visual motor stimulation. The pre- and post-stimulus OFF periods were constant for all four runs, set to be 40s and 100s respectively. The stimulus ON period varied between 20s, 40s, 80s and 120s across the runs (*c.f.* Figure 4.5). The stimulus blocks were repeated six times, four times, twice and once respectively, based on the duration of the stimulus ON period, so that the total simulation ON duration was approximately matched across all the runs.

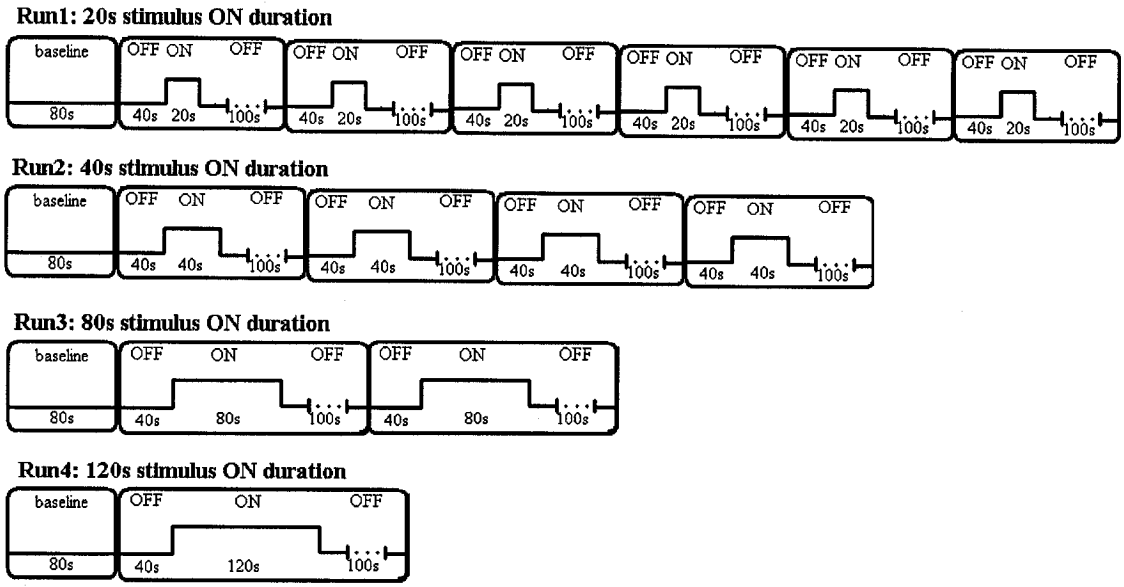

Figure 4.5: Design for Experiment #2. The functional experiment consisted of four runs. Each run began with a 80s baseline followed by OFF/ON/OFF visual and motor stimulation blocks. The pre- and post stimulus OFF periods were 40s and 100s respectively. The duration of the stimulation was varied between 20s, 40s, 80s and 120s across the four runs. The number of repetitions of stimulation blocks was also varied to maintain approximately equal overall stimulation time over the four runs.

4.2.2 MRI Data acquisition

All MR scans were performed on a 3.0 T Siemens Trio system. Subjects were immobilized using a head holder assembly. A receive-only birdcage head coil was used to

acquire functional and anatomical scans. The scanning protocol consisted of a high-resolution (1x1x2 mm^3) 3D RF-spoiled T1-weighted sequence for anatomical reference, followed by interleaved multi-slice QUIPSS II CBF and BOLD signal measurements respectively.

The high-resolution anatomical scan employed a TR of 23 ms, a TE of 7.4 ms, and non-selective 30° RF-spoiled excitation. This scan was used as an alignment reference for all functional scans and to localize the visual and motor cortices. The ASL-BOLD acquisition covered 12 slices (4x4x5 mm^3; inter-slice gap of 1mm) positioned parallel to the calcarine sulcus to include the motor and visual cortices. Figure 4.6 shows the CBF-BOLD interleaved protocol used for experiment #1. A similar protocol was used in experiment #2. CBF data was acquired using the QUIPSS II sequence [51], with two pre-saturation asymmetric bandwidth-modulated adiabatic selective saturation and inversion (BASSI) pulses [97] in the imaging region followed by an adiabatic BASSI inversion pulse in the labeling region (of thickness 100mm; gap of 10mm) and two BASSI QUIPSS II saturation pulses. The QUIPSS II delay (TI_1) was 700 ms and the post-label delay (TI_2) was 1300 ms. An EPI readout was employed with an echo time (TE) of 30 ms for BOLD and 23 ms for CBF and a repetition time (TR) of 2.0 s. The readout bandwidth was set at 2170 Hz/Px.

Informed consent was obtained from each subject prior to the scanning session. The experimental protocol was approved by the Research Ethics Board of the Montreal Neurological Institute.

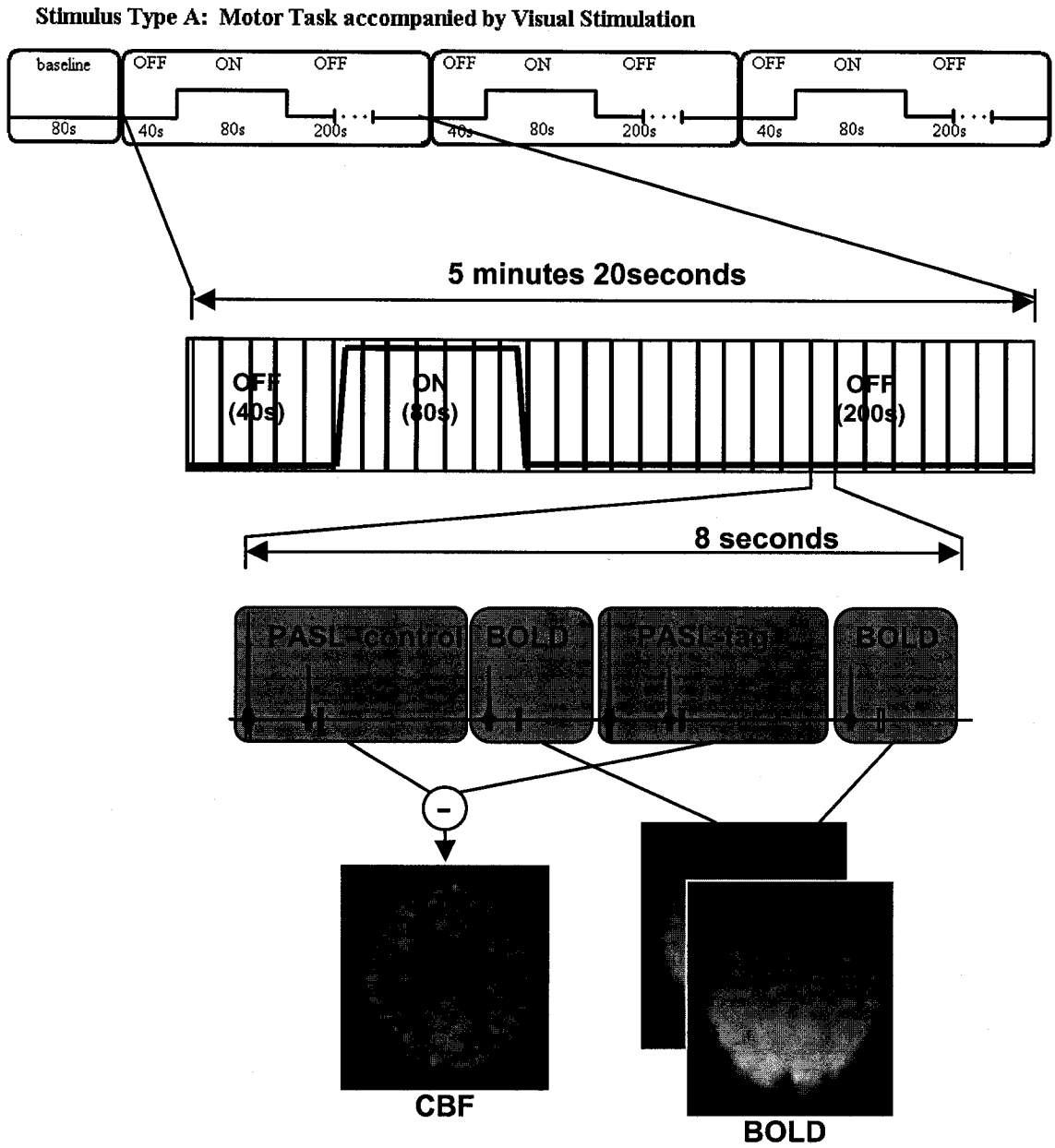

Figure 4.6: The CBF-BOLD interleaved fMRI protocol described for one run of experiment #1. The QUIPSS II / BOLD sequence contained two BOLD acquisitions, which give two successive BOLD images, interleaved with a slice selective and a non-selective ASL acquisition, the difference of which results in a flow-weighted QUIPSS II image.

4.2.3 Functional Image Analysis

The interleaved fMRI data was separated into BOLD and perfusion frames. The control and tag ASL images were subtracted to give CBF images. Motion parameters were estimated on the BOLD data set using AFNI's 3dvolreg software [98]. Frames with shifts greater than 1mm in the anterior-posterior, left-right or superior-inferior direction and rotations greater than 1° in the roll, pitch or yaw directions were omitted from further analysis. The data was spatially smoothed using a three dimensional Gaussian filter with a full-width-at-half-maximum (FWHM) of 6mm. Drift removal was performed by subtracting from each voxel's time course the low-frequency components of its discrete cosine transform, with a cutoff frequency of one half of the stimulation paradigm frequency. CBF images were obtained by subtracting the control and tag QUIPSS II images (*c.f.* Figure 4.6). Finally, the *fMRIstat* statistical package by K. Worsley et al. [99] was used to identify areas of statistically significant task correlated activation at an omnibus significance level of 0.05 in BOLD and CBF data. Regions of interest (ROI) were defined by thresholding the t-maps on an individual basis for each subject due to inter-subject slice placement variability. For each experiment two different methods of selecting the ROI were examined.

ROI selection criterion for Experiment #1: The first selection criterion involved identification of whole brain hypercapnia-correlated MR signal changes by thresholding the t-maps at $p<0.05$ for each of the two hypercapnia runs. Separate ROIs were obtained from BOLD and CBF data. Care was taken to ensure that the ROI corresponded to corticular regions alone by superimposing the ROI on the anatomical reference scan.

Activated voxels from the corpus callosum, thalamus (deep grey matter), of the cerebellum were masked out.

The second ROI selection criterion was restricted to voxels in the visual and motor regions alone. For the visual/motor stimulation run, BOLD and CBF ROIs were chosen by thresholding the corresponding t-maps at <0.05 significance level. These ROI2 maps were overlapped with the hypercapnia ROI1 maps (obtained using selection criterion 1) to isolate the subset of voxels within the visual cortex (VC) and the motor cortex (MC) that showed hypercapnia correlated change for the 5% and 10% hypercapnia runs. Separate ROIs were selected for the VC and MC for BOLD and CBF data. In all cases, care was taken to ensure that the ROI corresponded to the appropriate anatomical region on the cortex by superimposing the ROI on the anatomical reference scan.

ROI selection criterion for Experiment #2: The first set of BOLD and CBF ROIs were selected by thresholding the individual t-maps for each of the four functional runs at a $p<0.05$ significance level. The visual and motor cortex ROI's were separated from each other. ROIs defined in this manner varied slightly in extent between the four runs for the same subject due to the difference in the stimulus ON duration.

The second region was defined by selecting the subset of voxels that were common to both the BOLD and CBF ROI maps obtained via criterion 1 above. Two common BOLD-CBF ROI map, one each for the visual and motor regions, were obtained for each of the four runs pertaining to the same subject. Since the BOLD signal reflects oxygenation changes in and around capillary and venous vessels [79, 100], and the ASL technique isolates signal from the arteriolar, capillary, tissue and arterial signal [45], the voxels contained in ROI2 should represent microvascular areas.

4.2.4 Time Course Analysis

Average ROI time courses were calculated for each subject and stimulus conditions for each of the two experiments by averaging across the repetitions in stimulation blocks. The mean positive amplitude of the functional response was obtained by averaging the signal intensity across all steady state activation frames. The steady state frames included the entire set of activation frames in the stimulus ON epoch following the first 8s and 20s after commencement of the stimulus ON period for experiments #1 and #2 respectively.

To observe and quantify the occurrence of the BOLD and CBF transients, the time course data for each subject was fitted with the hemodynamic response function (HRF) convolved with the stimulus paradigm. This function incorporates both the steady state and the transient change in the BOLD and CBF data. The HRF, as described by Glover et al [101], is modeled as the difference of two gamma density functions:

$$\gamma_1(t) = \left(\frac{t}{p_1}\right)^{\frac{8.p_1^2.\log(2)}{p_2^2}} .e^{\frac{-(t-p_1)}{p_2^2/(8.p_1.\log(2))}} \tag{4.1}$$

$$\gamma_2(t) = \left(\frac{t}{p_3}\right)^{\frac{8.p_3^2.\log(2)}{p_4^2}} .e^{\frac{-(t-p_3)}{p_4^2/(8.p_3.\log(2))}} \tag{4.2}$$

$$HRF = \gamma_1 - p_5.\gamma_2 \tag{4.3}$$

The parameters p_1 and p_2 represent the time-to-peak and the FWHM of the first gamma density function, p_3, p_4, and p_5 represent the time to peak, FWHM and the amplitude modulation coefficient of the second gamma density function. A minimum sum of squared error fitting technique was used to fit for all five parameters. To overcome fitting errors due to noise in the CBF time courses, all time courses were filtered with a hanning

window of FWHM of 20s before the fitting. The fitting was done in two steps; initially the pre-stimulus OFF and stimulus ON epochs were fitted, in order to model a possible initial dip and the initial overshoot. Following this step, the stimulus ON and the post-stimulus OFF epochs were fitted, allowing for the independent modeling of the post-stimulus transient characteristics. Finally, the two fitting functions were combined and plotted with the average time course data to give an average fit for the entire time course.

Two time course parameters were measured from the fits obtained on the BOLD and CBF data: the maximum amplitude and the duration of the post-stimulus undershoot. The maximum amplitude was defined as the minima of fitted function after the cessation of the stimulus. The duration of the undershoot was defined as the time that elapsed between when the post-stimulus signal drops below and recover to 95% of its maximum negative amplitude. It should be noted that the low-pass filtering performed, in addition to smoothing out the high frequency peaks in the functional time courses, prolongs the duration of the fitted post-stimulation undershoot. The FWHM of the low-pass filtered undershoot is equal to the square root of the sum of squares of the FWHM of the undershoot and the FWHM of the window used in performing for low-pass filtering. This occurrence is of little consequence in this thesis as the undershoot duration parameter was used to compare between the time courses obtained under different stimulation/ hypercapnia conditions, all data being processed in a similar manner.

Finally, ANOVA analysis was performed on the time course parameters for each of the two experiments to establish the relationship between the various stimulation conditions and each of the time course parameters. For experiment #1, the statistics revealed if the parameter values were affected differently by the hypercapnia condition versus the visual and motor stimulation, while for experiment #2, the effect of varying the

stimulation duration was assessed. Additionally, the ANOVA revealed if the visual cortex data significantly differed from that of the motor cortex. The simple main effect test and the Tukey's pair-wise comparison test were used for post hoc analysis. Separate analysis was done for time courses corresponding to each of the two ROIs in each experiment.

Chapter 5

Experiment #1 Results

For this experiment, 11 healthy volunteers were scanned using an fMRI protocol consisting of three CBF-BOLD interleaved runs. During one of the runs, the subject was presented with a visual stimulus and motor task, while for the other two runs, the stimulus consisted of 5% and 10% hypercapnia blocks. Each run contained three repetitions of the same stimulus condition. All subjects successfully completed the experiment.

In all subjects, stimulus induced changes in the BOLD and the CBF signal were observed in the visual and motor cortices for the visual/motor stimulation run and throughout the cortex for the hypercapnia runs.

The end tidal CO_2 ($ETCO_2$) and respiratory rates were measured for all subjects throughout the hypercapnia scans. Two different 3D ROI types were defined for each subject and the average time courses were calculated for each ROI. In this chapter the summarized values of the physiological monitoring and average ROI volumes are presented for each of the stimulus conditions for BOLD and CBF data. Following this, the average time courses are described. Statistical analysis was performed to explore the nature of the post-stimulus undershoot in the hypercapnia data. Finally, a comparison

between the time course parameters obtained from the normocapnia and the hypercapnia data was used to probe underlying physiological relationships.

5.1 Physiological Monitoring

The $ETCO_2$ and respiratory rates during the two-hypercapnia conditions compared with normocapnia values are given in Table 5.1. The subjects maintained a reasonably constant respiratory rate of about 16 breaths/minute; therefore the changes in $ETCO_2$ readings should reflect CO_2 variations in arterial blood. While $ETCO_2$ was relatively constant during the normocapnia condition, an increase of a ~6 and 15 mmHg was observed during 5% and 10% hypercapnia, confirming the presence on elevated CO_2 levels in blood.

	Normocapnia	5% Hypercapnia	10% Hypercapnia
$ETCO_2$(mm Hg)	40.23 ± 0.53	45.75 ± 0.78	55.16 ± 1.45
Respiration rate (breaths/min)	16.17 ± 0.78	16.12 ± 1.08	16.95 ± 1.79

Table 5.1: Summary of the average (± standard error) physiological values over all subjects.

5.2 Region of Interest

Two ROIs used for time course analysis were described in detail in the methods section. For this experiment, ROI1 comprised of whole brain activation regions for the two hypercapnia conditions, was obtained by thresholding the t-maps from the 5% and 10% hypercapnia runs at a <0.05 significance level. Figure 5.1 shows sample ROI1 BOLD and CBF maps defined for one subject.

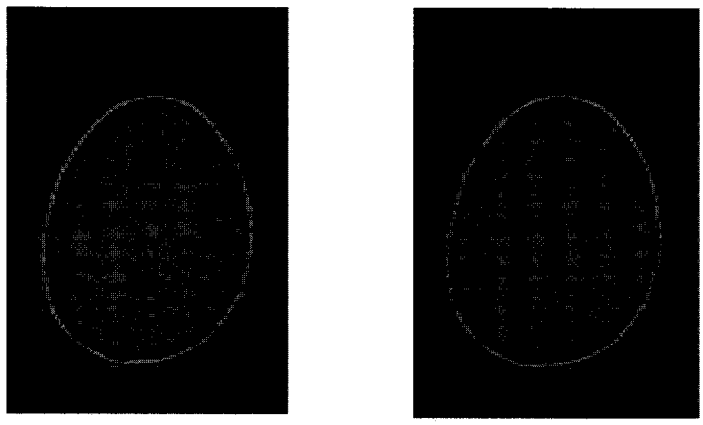

BOLD whole-brain t-map CBF whole-brain t-map

(A) 5% hypercapnia condition

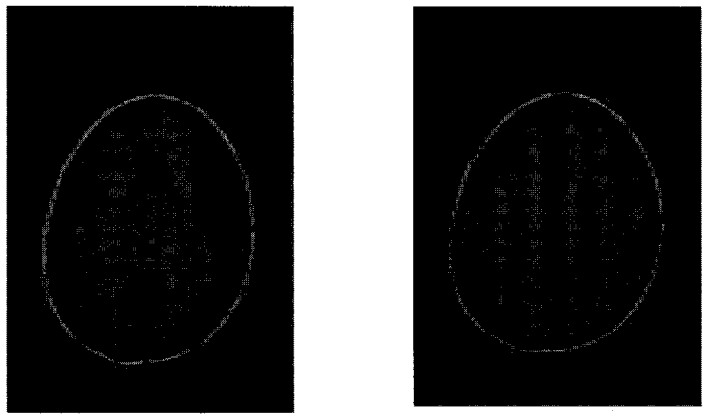

BOLD whole-brain t-map CBF whole-brain t-map

(B) 10% hypercapnia condition

Figure 5.1: Whole brain ROI1 (shown in red) defined for a sample subject. The BOLD and CBF t-maps for the (A) 5% and (B) 10% hypercapnia conditions are shown, after applying <0.05 significance threshold.

Significant activation was seen throughout the cortex, mainly restricted to grey matter areas. The visual/motor stimulation run was not analyzed using this ROI criterion. This particular ROI was used primarily for qualitative observation of global BOLD and CBF time courses arising from the CO_2 inhalation.

ROI2 was restricted to regions in the visual/motor cortices. The visual/motor stimulation run, ROI2 was chosen by thresholding the t-maps at <0.05 significance level. For the hypercapnia data, the thresholded t-maps from the visual/motor run were

overlapped with the hypercapnia t-maps to isolate voxels from with in the VC and MC that showed significant hypercapnia induced signal changes. Figure 5.2 shows ROI2 BOLD and CBF maps defined for one subject's motor cortex. This ROI was used to compare hypercapnic time courses with visual/motor activation time courses.

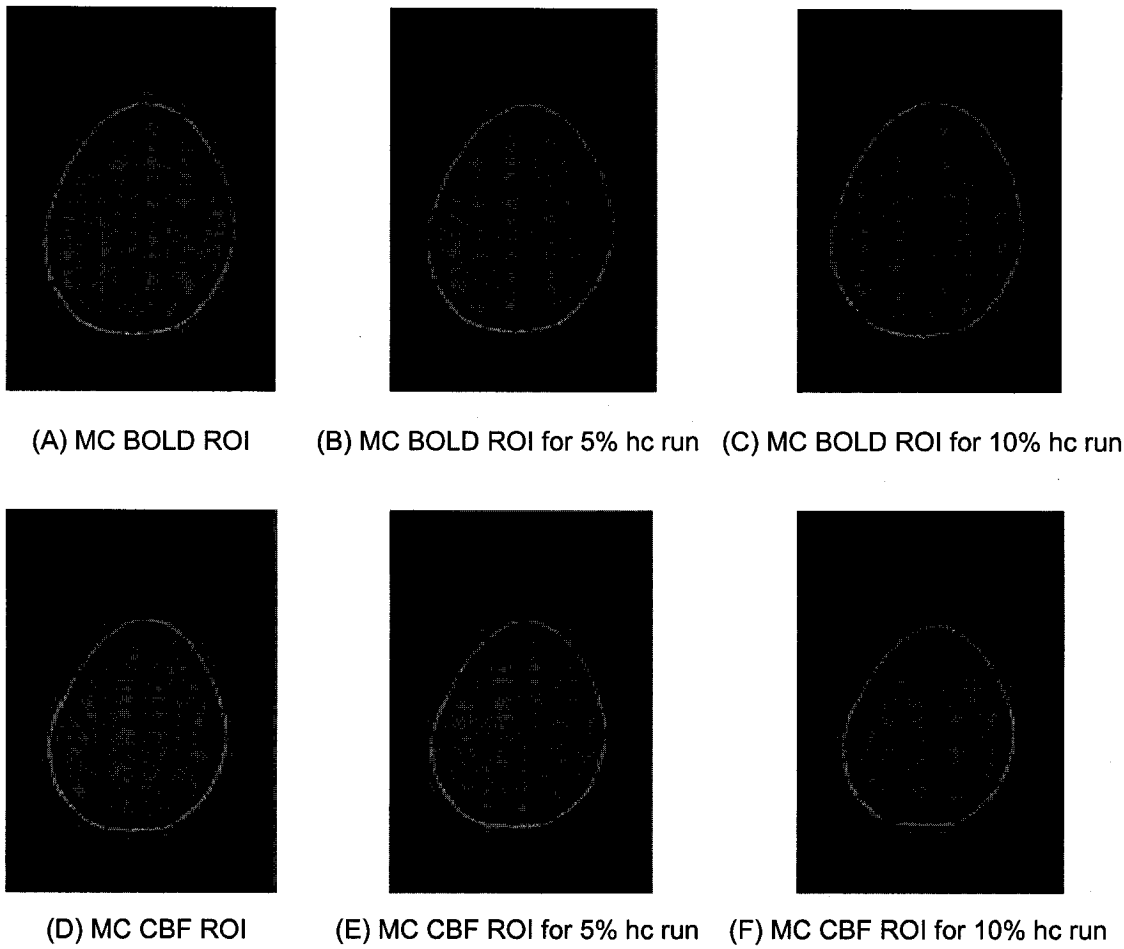

(A) MC BOLD ROI (B) MC BOLD ROI for 5% hc run (C) MC BOLD ROI for 10% hc run

(D) MC CBF ROI (E) MC CBF ROI for 5% hc run (F) MC CBF ROI for 10% hc run

Figure 5.2: Motor cortex ROI2 (shown in red) defined for a sample subject. (A) and (D) show thresholded BOLD and CBF maps from the visual /motor stimulation run respectively; (B) and (E) show the ROI2 BOLD and CBF maps obtained by selecting the subset of voxels showing activation in both the motor and the 5% hypercapnia thresholded t-maps; (C) and (F) show the ROI2 BOLD and CBF maps obtained by selecting the subset of voxels showing activation in both the motor and the 10% hypercapnia thresholded t-maps.

ROI1 (11 subjects)		5% Hypercapnia	10% Hypercapnia
	BOLD	165.01 ± 34.45	214.77 ± 38.23
	CBF	10.02 ± 2.05	41.59 ± 10.03

ROI2		Functional run	5% hypercapnia	10% hypercapnia
Visual Cortex	BOLD	12.77 ± 1.50	3.33 ± 1.32	4.98 ± 1.61
	CBF	4.25 ± 0.73	*0.32 ± 0.06	‡1.91 ± 0.61
Motor Cortex	BOLD	18.38 ± 1.72	6.55 ± 2.24	10.77 ± 2.78
	CBF	4.11 ± 0.65	†0.14 ± 0.03	*0.22 ± 0.04

Table 5.2: Mean ROI volumes (in cc ± standard error) for ROI1 and ROI2 averaged over all subject (n=11) except where noted († n=5, *n=7, ‡n=10).

Due to the low SNR of the CBF data, some of the subjects failed to show any voxels with clear hypercapnic and CBF activations. As a result only seven and ten subject visual cortex ROIs for the 5% and 10% hypercapnia runs were possible, while for the motor cortex regions, only five and seven subject ROIs were used for ROI2 time course analysis. Table 5.2 shows the average ROI volumes for each ROI selection criterion used in time course analysis.

5.3 Activation Time Course Analysis

The time courses for BOLD and CBF data were obtained by averaging all voxels within the ROI for each time point in the experimental run. In this experiment, stimulation blocks were repeated three times per stimulation condition; the time course data was

averaged across the repeated blocks to give average time courses for each stimulation condition.

The MRI signal changed with the hypercapnic manipulations following a slight observable delay. This time delay can be explained by the time between the gas exchange in the lungs and the subsequent change in the cerebral blood oxygenation. Similarly, after the cessation of the CO_2 enriched air, the BOLD and CBF signals returned to baseline following a delay.

The average positive response parameter was obtained by averaging the MR signal over all frames during the stimulus ON period following the first 20s after the commencement of the stimulus. The first 20s were omitted to allow for the delayed hypercapnia response to reach its steady state value. The average time courses were then low pass filtered using a hanning window with FWHM of 20s and fitted with the HRF function convolved with the stimulation paradigm. This was done to facilitate the quantification of two additional time course parameters: the maximum amplitude of the post-stimulus undershoot (the local post-stimulus minima in the fitted HRF) and the maximum duration of the post-stimulation undershoot (the time taken for the fitted HRF to drop below and return to 95% of the maximum undershoot value). In the few cases where individual subject time courses failed to show the undershooting phenomenon, the maximum amplitude and duration of the undershoot was set to zero for inclusion in the statistical analysis.

5.3.1 ROI1: Analysis of whole-brain hypercapnic time courses

Sample whole brain BOLD and CBF time courses corresponding to the 5% and 10% hypercapnia runs for one subject are shown in Figure 5.3.

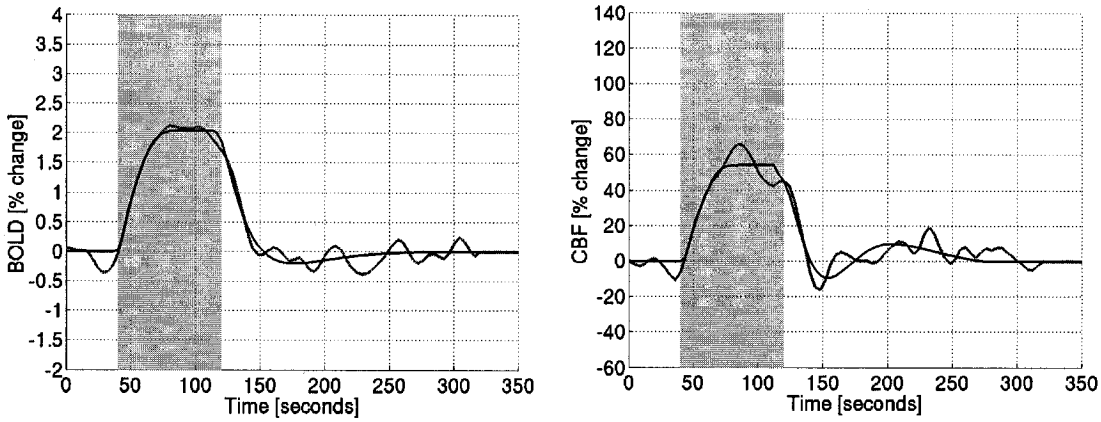

(A) 5% hypercapnia

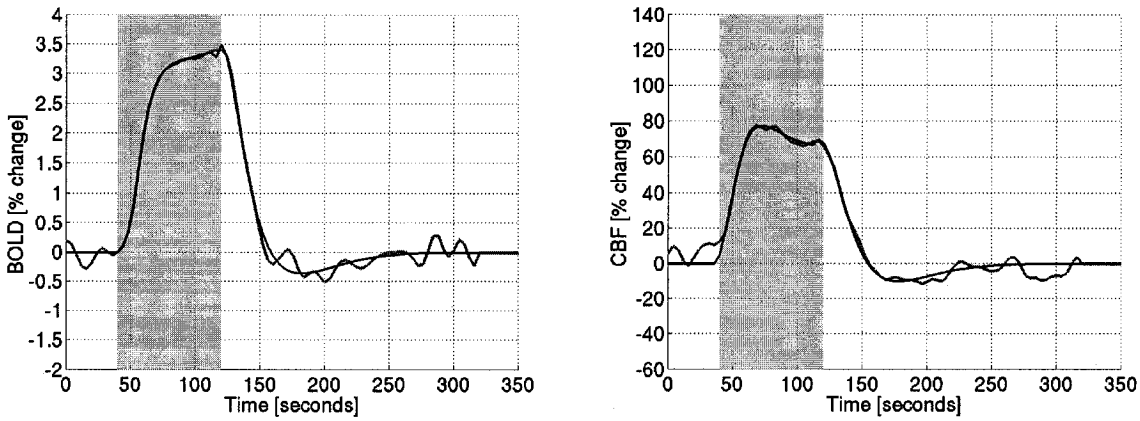

(B) 10% hypercapnia

Figure 5.3: BOLD (left) and CBF (right) time courses for the (A) 5% hypercapnia and (B) 10% hypercapnia conditions from a sample subject's ROI1. The shaded region signifies the hypercapnia ON period. The curve shown in red represents the temporally filtered (hanning window with FWHM of 20s) time course from the functional data while the black curve represents the HRF fitted to the data.

The average positive BOLD response increased significantly between the 5% and 10% hypercapnia condition (from $1.73 \pm 0.15\%$ to $3.38 \pm 0.27\%$, $F(1,20)=29.06$, $p<0.0001$). However, the increase in the CBF response was not significant (from $56.52 \pm 6.55\%$ to $60.28 \pm 4.36\%$, $F(1,20)=0.23$, $p>0.05$). Table 5.3 summarizes the three time course parameter values for ROI1 BOLD and CBF data.

ROI1 (11 subjects)		**5% hypercapnia**	**10% hypercapnia**
Average positive response	BOLD	1.73 ± 0.15	3.38 ± 0.27
[% change]	CBF	56.52 ± 6.55	60.28 ± 4.36
Maximum undershoot amplitude	BOLD	-0.20 ± 0.06	-0.28 ± 0.07
[% change]	CBF	-13.37 ± 3.75	-7.23 ± 1.97
Undershoot duration	BOLD	56.72 ± 15.78	67.64 ± 16.52
[seconds]	CBF	55.63 ± 15.44	71.27 ± 16.84

Table 5.3: Summary of whole brain BOLD and CBF time course parameters averaged over all subjects (n=11).

For the BOLD time course, clear post-stimulus undershoots were observed in the data from 7 subjects for the 5% and 10% hypercapnia conditions; while for the CBF data, 8 showed undershooting under the two conditions. Table 5.5 summarizes this information. Statistical analysis showed that the maximum undershoot amplitude and duration did not vary significantly between the two hypercapnia conditions ($F(1,20)<2.11$, $p>0.05$) in either BOLD (mean of $-0.24 \pm 0.05\%$ lasting 62.18 ± 15.86 seconds) or CBF data (mean of -10.30 ± 2.17 lasting 63.45 ± 11.28seconds).

5.3.2 ROI2: Analysis of functional and hypercapnic time courses from the visual and motor cortex regions

Average time course data was calculated for the visual/motor stimulation run and the hypercapnia runs from regions restricted to the visual and motor cortices. The BOLD time courses showed clear stimulation correlated changes in both the visual and motor cortex for all three-stimulus conditions. The CBF time courses although more noisy than the BOLD, showed a similar stimulus correlated pattern. Figure 5.4 shows the visual cortex BOLD and CBF ROI2 time courses from the visual stimulation and the two hypercapnia runs for a sample subject.

Table 5.4 summarizes the three time course parameter values for ROI2 BOLD and CBF data. The BOLD average positive response was consistently higher in the visual cortex then in the motor cortex (mean of $3.61 \pm 0.48\%$ and $2.17 \pm 0.19\%$ respectively, $F(1,10)=17.21, p<0.005$) and was significantly higher during the 10% hypercapnia run as compared with the visual/motor stimulation and the 5% hypercapnia run (mean of 4.19 ± 6.64 % and $\sim 2.23 \pm 0.19$ % respectively, $F(2,20)=8.09$, $p<0.005$).

An unequal N's ANOVA revealed that the average positive CBF response was higher in the motor cortex as compared with the visual cortex (mean of $76.76 \pm 7.21\%$ and $51.84 \pm 3.85\%$ respectively, $F(1,43)=6.85$, $p<0.05$). Further, the CBF response increased significantly between the 5% hypercapnia run and the other two runs (mean of $42.79 \pm 4.86\%$ and $68.89 \pm 4.89\%$ respectively, $F(2,43)=4.76$, $p<0.05$).

For the visual/motor stimulation BOLD time courses, eight of the eleven subjects showed clear undershooting in the visual cortex, while seven showed a clear undershoot in the motor cortex ROI. For the CBF data of the same run, five and eight undershoots were seen in the visual and motor cortex time courses respectively. For the 5%

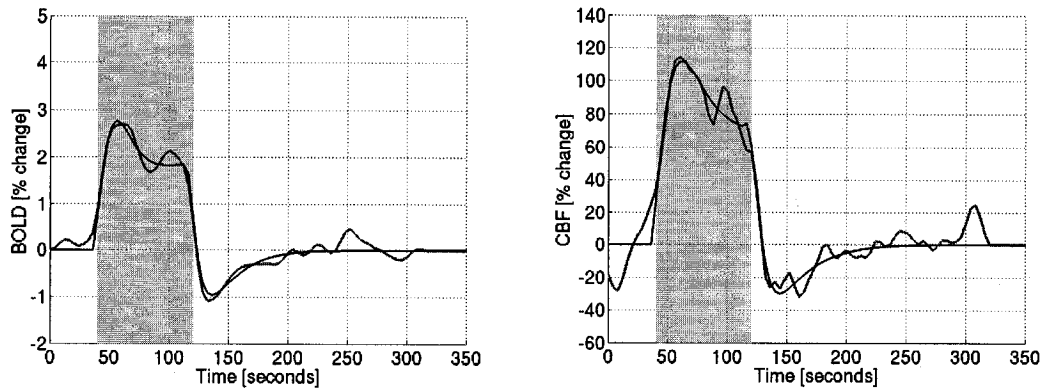

(A) Visual stimulation

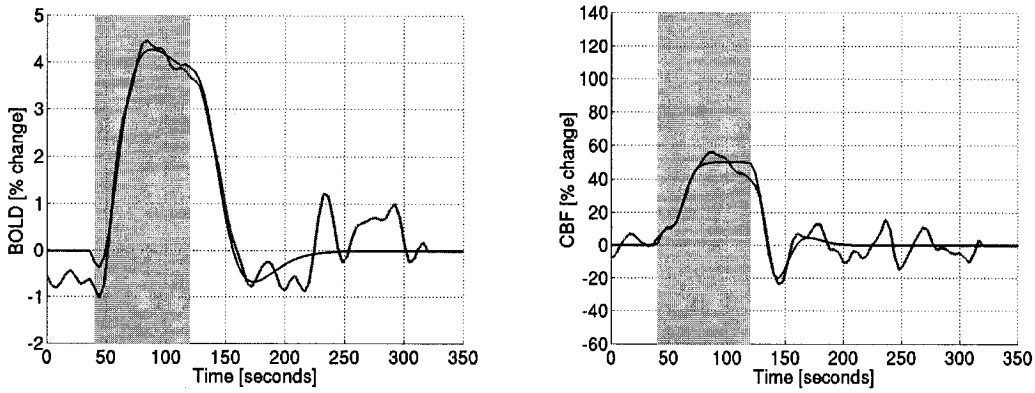

(B) 5% hypercapnia

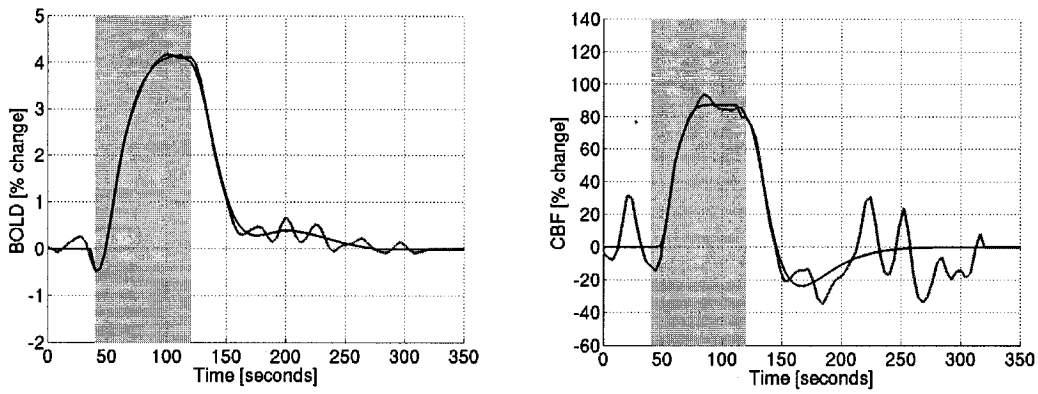

(C) 10% hypercapnia

Figure 5.4: BOLD (left) and CBF (right) ROI2 time courses for (A) the visual stimulus, (B) the 5% hypercapnia, and (C) the 10% hypercapnia conditions from a sample subject. The shaded region signifies the stimulus ON period. The curve shown in red represents the temporally filtered (hanning window with FWHM of 20s) time course from the functional data while the black curve represents the HRF fitted to the data.

hypercapnia data, five and four subjects showed clear BOLD undershoots, while five and four showed CBF undershoots in the visual and motor cortices respectively. For the 10% hypercapnia data set, a total of four subjects showed BOLD post-stimulus undershooting in both brain regions, while six and five subjects showed CBF undershooting in the visual and motor cortices respectively. Table 5.5 summarizes this information.

The amplitude and the duration of the BOLD undershoots did not vary either between the brain regions ($F(1,10)<1.7$, $p>0.05$) or between visual/motor stimulation, 5% and 10% hypercapnia conditions (mean of $-0.28 \pm 0.05\%$ lasting 33.52 ± 5.40 seconds, $F(2,20)<0.09$, $p>0.05$). Similarly, the CBF undershoots did not differ significantly with brain regions ($F(1,43)<1.15$, $p>0.05$) or between the three stimulation types (mean of -16.44 ± 2.35 % lasting 50.04 ± 7.43 seconds, $F(2,43)<1.26$, $p>0.05$).

ROI2(11 subjects)			Visual / motor stimulation	5% hypercapnia	10% hypercapnia
Average positive response [% change]	Visual cortex	BOLD	2.16 ± 0.35	3.39 ± 0.51	5.27 ± 1.17
		CBF	53.45 ± 5.61	40.09 ± 4.38	59.02 ± 8.08
	Motor cortex	BOLD	1.75 ± 0.15	1.63 ± 0.18	3.12 ± 0.38
		CBF	85.30 ± 6.32	47.52 ± 11.74	80.06 ± 18.04
Maximum undershoot amplitude [% change]	Visual cortex	BOLD	-0.47 ± 0.13	-0.41 ± 0.25	-0.16 ± 0.09
		CBF	-8.06 ± 3.30	-20.34 ± 7.27*	-16.00 ± 4.16‡
	Motor Cortex	BOLD	-0.25 ± 0.08	-0.17 ± 0.06	-0.22 ± 0.10
		CBF	-17.34 ± 5.20	-21.33 ± 7.14†	-21.99 ± 9.22*
Undershoot duration [seconds]	Visual cortex	BOLD	35.64 ± 10.72	21.09 ± 10.82	27.64 ± 14.03
		CBF	33.44 ± 15.58	35.43 ± 15.38*	67.56 ± 20.25‡
	Motor cortex	BOLD	26.55 ± 11.00	18.55 ± 9.68	37.82 ± 15.85
		CBF	40.36 ± 13.90	78.00 ± 31.85†	67.42 ± 23.49*

Table 5.4: Summary of ROI2 BOLD and CBF time course parameters averaged over all subjects (n=11) except where indicated (†n=5, *n=7, ‡n=10).

ROI1 (11 subjects)		5% Hypercapnia	10% Hypercapnia
	BOLD	7	7
	CBF	8	8

ROI2 (11 subjects)		Visual / motor	5% hypercapnia	10% hypercapnia
Visual cortex	BOLD	8	6	4
	CBF	5	5*	6‡
Motor cortex	BOLD	7	6	4
	CBF	8	4†	5*

Table 5.5: Summary of the number of post-stimulus undershoots seen amongst the time courses for each ROI and brain region. (‡ from a total of 10 time courses, * from a total of 7 time courses, and, † from a total of 5 time courses)

Chapter 6

Experiment #2 Results

For this experiment, 10 health volunteers were scanned using an fMRI protocol consisting of four CBF-BOLD interleaved runs during which time the subject was presented with a visual stimulus and motor task of varying duration. The stimulation duration was varied between 20s, 40s, 80s and 120s across the four fMRI runs.

Stimulus induced changes in the BOLD and the CBF signal were observed in the visual and motor cortices of each subject. Data from one subject was dropped due to excessive head motion during the 120s stimulation run.

For comparison of the four stimulation duration conditions with one another, two different 3D ROI types were defined for each subject and the average time courses were calculated for each ROI. In this chapter the average ROI volumes are presented for each of the stimulus conditions (brain region and stimulation duration) for BOLD and CBF data. Following this, the average time courses are described. The relationship between various time course parameters and stimulus duration is analyzed for visual and motor cortex ROIs.

6.1. Region-of-Interest Analysis

The two ROIs used for the comparison of BOLD and CBF changes were described in the methods section. ROI1 consisted of individual masks for each of the four runs, obtained by separately thresholding the BOLD and CBF t-maps at a <0.05 significance level. ROI2 comprised the subset of voxels that showed statistically significant activation in both the BOLD and CBF t-maps.

One subject failed to show any voxels in the activation-correlated t-maps for the 20s and 40s stimulation duration runs. This was attributed to the low CNR of the subject's data compared with other subjects in the study. The same subject failed to produce a ROI2 mask as the BOLD and CBF t-maps contained no common voxels in the visual cortex. As a result, this subject was excluded from further analysis. Additionally, due to the limited extent of the CBF t-maps from the 20s stimulation runs, several subjects failed to show intersecting BOLD and CBF voxels. As a result, an uneven number of subjects were analyzed for the four stimulation runs using ROI2 analysis. The typical ROIs obtained for one subject for the visual cortex are displayed in Figure 6.1. Table 6.1 summarizes the average ROI volumes across all subjects for ROI1 and ROI2.

6.2 Activation Time Courses

The time courses for BOLD and CBF data were obtained by averaging all voxels within the ROI for each time point in the experimental run. If the stimulation block was repeated more than once during a given stimulus condition, the time course was averaged across the repeated blocks to give an average time course for each subject. Post-stimulus

ROI1 (8 subjects)		20s	40s	80s	120s
Visual cortex	BOLD	3.46±0.88	8.67±2.41	8.00±2.68	7.5±2.14
	CBF	1.91±0.58	4.43±0.66	5.31±1.48	3.84±1.15
Motor cortex	BOLD	4.26±1.21	10.12±1.95	8.91±1.54	9.57±2.53
	CBF	2.07±0.78	2.76±0.97	3.44±0.87	2.71±0.92

ROI2	20s	40s	80s	120s
Visual cortex	0.92±1.15‡	3.77±1.24	4.68±2.02	3.81±1.73*
Motor cortex	0.88±0.22†	1.72±0.46	2.05±0.51	2.38±1.09*

Table 6.1: Average ROI volumes (in cc±standard error) for ROI1 and ROI2. The volumes were averaged over 8 subjects except where indicated (‡n=4, †n=6, *n=7).

undershoots were seen in the BOLD and CBF time courses in both visual and motor cortex data, for both ROIs in most of the subjects.

The average positive response was obtained by averaging the MR signal over all frames following the first 8s during the stimulus ON period of the average time course. The average time courses were then temporally filtered with a hanning window of FWHM 20s (5 frames) and fitted with the HRF function convolved with the stimulation paradigm. This was done to facilitate the quantification of two additional time course parameters: the maximum amplitude of the post-stimulus undershoot (the local post-stimulus minima in the fitted HRF) and the maximum duration of the post-stimulation undershoot (the time taken for the fitted HRF to drop below and return to 95% of the maximum negative undershoot value). In the cases where individual subject time courses

ROI 1: Individual BOLD and CBF ROIs for each stimulation condition

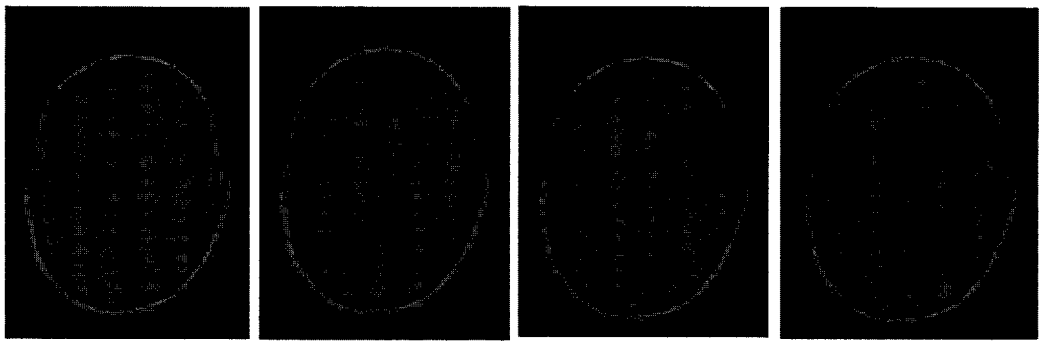

20s 40s 80s 120s

(A) VC BOLD t-maps

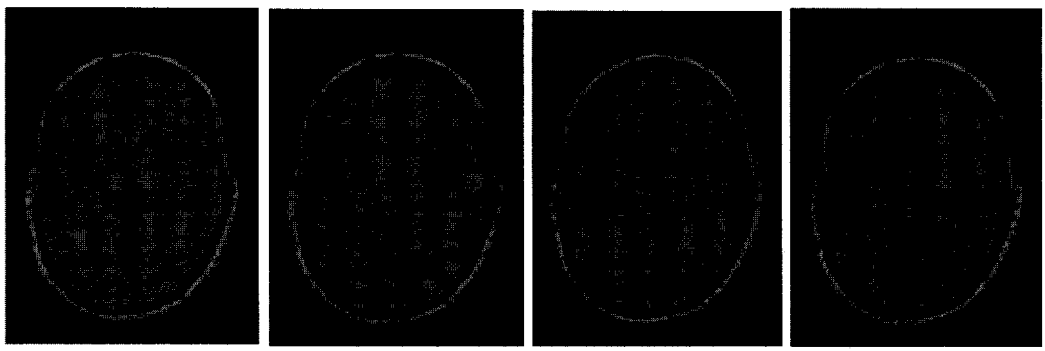

20s 40s 80s 120s

(B) VC CBF t-maps

ROI 2: Intersection of BOLD and CBF t-maps for each stimulation condition

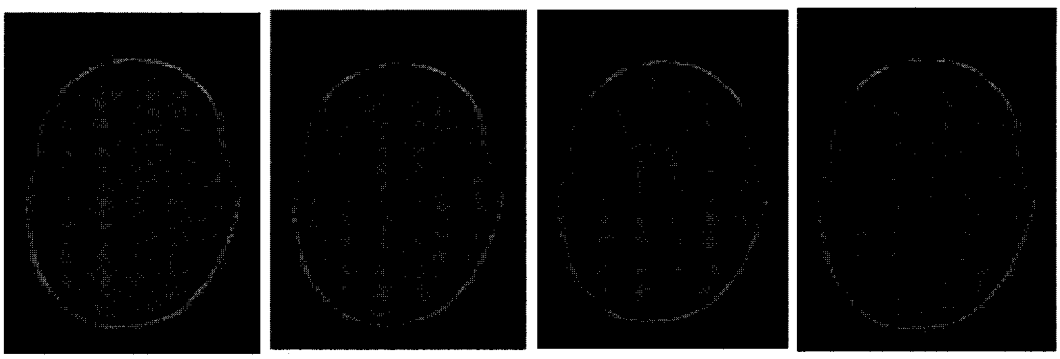

20s 40s 80s 120s

(C) VC BOLD and CBF intersection maps

Figure 6.1: Visual cortex ROIs (shown in red) defined for a sample subject. (A) and (B) show visual cortex BOLD and CBF ROIs for each experimental condition chosen using ROI1 criterion; (C) shows visual cortex ROI2s formed by intersecting the ROI1 BOLD and CBF t-maps.

failed to show the undershooting phenomenon the maximum amplitude and duration of the undershoot was set to zero for inclusion in the statistical analysis. The two ROIs were analyzed separately to assess the relationship between the three time course parameters and stimulation duration.

6.2.1 ROI1: Analysis of functional data using individual run ROIs

Sample BOLD and CBF time courses for the four stimulation conditions obtain from one subject's visual cortex ROI1 are shown in Figure 6.2 and 6.3 respectively. All eight subjects showed clear undershoots under each stimulation condition for the visual cortex BOLD time courses, while for the motor cortex BOLD data, seven, four, five and seven of the eight subject time courses showed undershoots for the 20s, 40s, 80s and 120s stimulation duration condition respectively. For the visual cortex CBF data, clear undershoots could be seen in all eight time courses for the 20s and the 80s stimulation condition, while only seven subjects showed undershooting under the 40s and 120s stimulation conditions. In the motor cortex CBF data, undershoots were observed in eight, seven, six and seven of the subject time courses under the four stimulation duration conditions respectively. This data is summarized in Table 6.8.

Average positive response: Table 6.2 summarizes the average positive response of the ROI1 time courses averaged over all subjects.

The average positive response of the BOLD time course differed significantly with stimulation duration ($F(3,21)=8.91$, $p<0.001$), but not with brain region ($F(1,7)=1.75$, $p>0.05$). Post hoc tests revealed that the maximum amplitude dropped significantly between the 20s and 40s, the 20s and 80s and the 120s and 40s stimulation

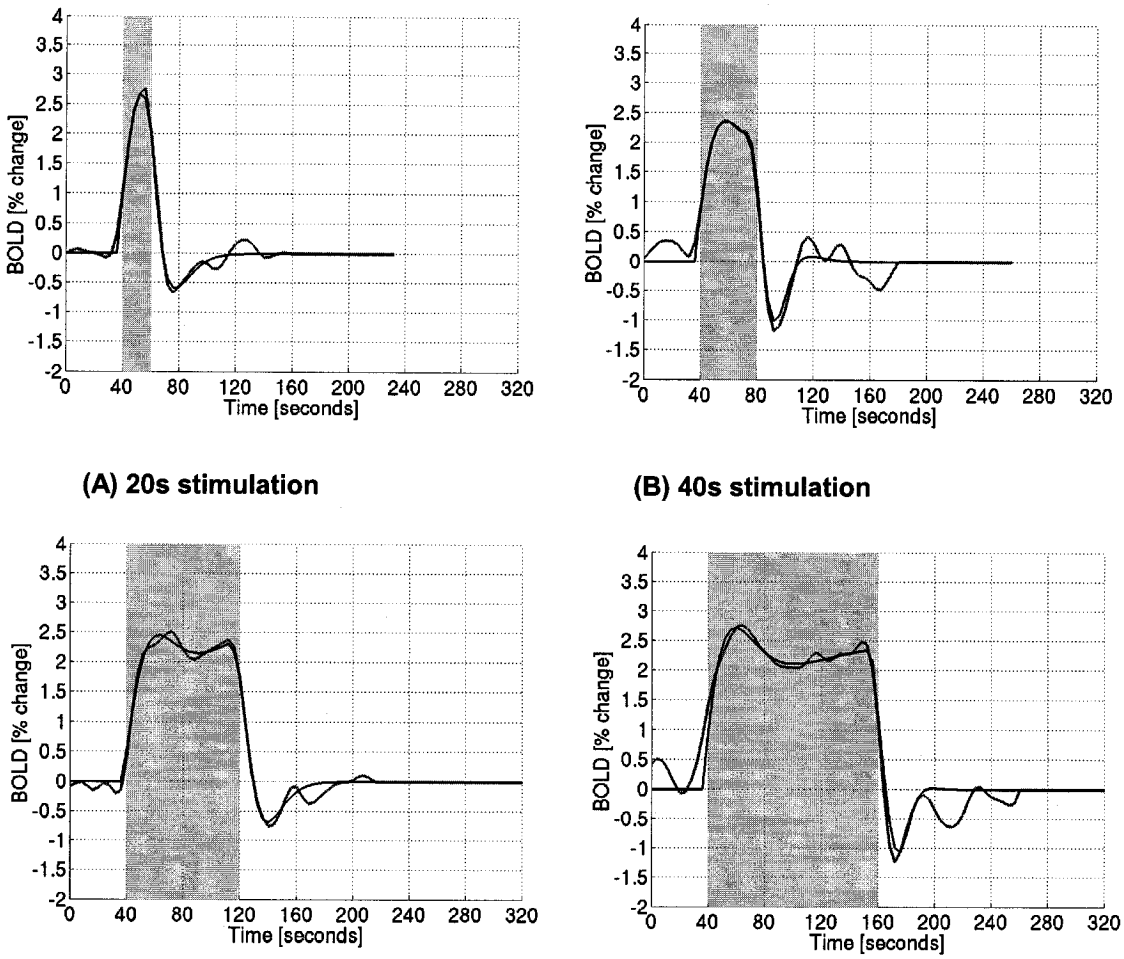

Figure 6.2: BOLD time courses for the four stimulation conditions obtained from a sample subject's visual cortex ROI1 data. The shaded region signifies the stimulus ON period. The curve shown in red represents the time course from the temporally filtered (hanning window with FWHM of 20s) functional data while the black curve represents the HRF fitted to the data.

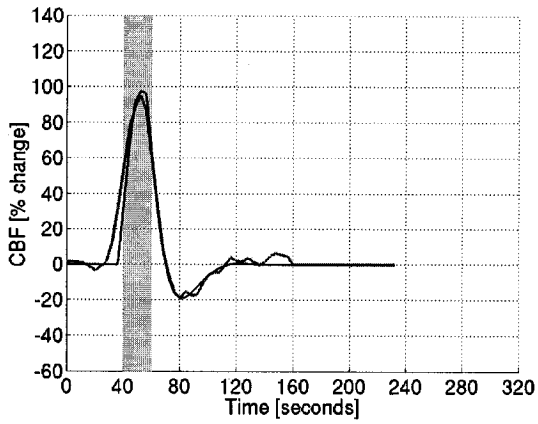

(A) 20s stimulation

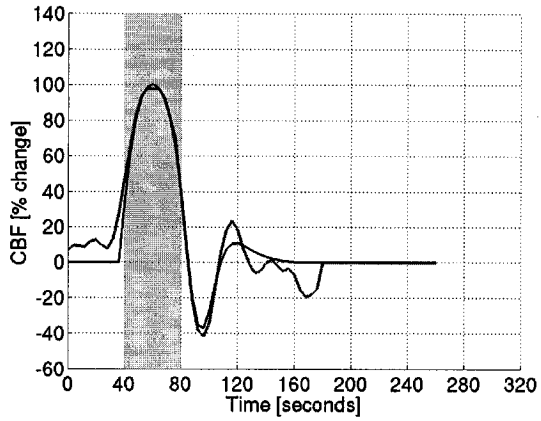

(B) 40s stimulation

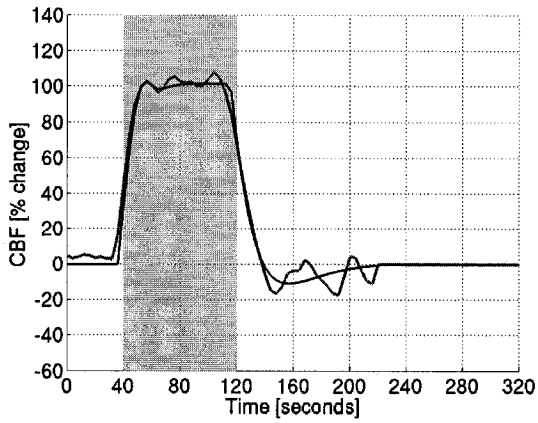

(C) 80s stimulation

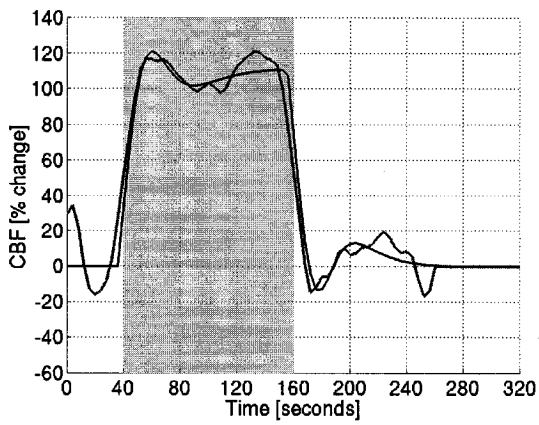

(D) 120s stimulation

Figure 6.3: CBF time courses for the four stimulation conditions obtained from a sample subject's visual cortex ROI1 data. The shaded region signifies the stimulus ON period. The curve shown in red represents the time course from the temporally filtered (hanning window with FWHM of 20s) functional data while the black curve represents the HRF fitted to the data.

ROI1 (8 subjects)		20s	40s	80s	120s
Visual cortex	BOLD	2.80±0.26	1.92±0.10	1.94±0.21	2.65±0.23
	CBF	61.69±6.00	69.11±5.23	66.80±11.31	81.85±5.42
Motor cortex	BOLD	2.28±0.40	1.67±0.16	1.89±0.24	1.96±0.12
	CBF	51.20±8.66	79.92±10.26	85.40±9.92	90.38±10.95

Table 6.2: The maximum positive amplitude of the BOLD and CBF response (in % change ± standard error) for visual and motor cortex ROI1 time courses averaged over all subjects.

duration conditions (mean of 2.52±0.24%, 1.80±0.10%, 1.92±0.16%, 2.30±0.16% for the 20s, 40s, 80s and 120s conditions respectively, $p<0.05$).

Similarly for the CBF data, the average positive response differed significantly with stimulation duration ($F(3,21)=5.48, p<0.01$) but not with brain region ($F(1,7)=0.58$, $p>0.05$). Further analysis revealed that the average positive response for the 20s stimulation (mean of 56.35±5.27%) time course was significantly lowed than the 120s stimulation condition (mean of 86.12±6.00%, $p<0.01$). No other effects were significant (mean CBF response of 72.55±3.29%).

Maximum undershoot amplitude: Table 6.3 summarizes the maximum undershoot amplitude of ROI1 time courses averaged over all subjects.

Statistical analysis performed on the data revealed that post-stimulus undershoot in the visual cortex was significantly more pronounced (deeper) then that in the motor cortex ($F(1,7)>8.14$, $p<0.05$) for both the BOLD (means of –0.73±0.08% and –0.40±0.07% for the visual and the motor cortex respectively) and CBF

ROI1 (8 subjects)		20s	40s	80s	120s
Visual cortex	BOLD	-0.75±0.16	-0.62±0.09	-0.98±0.17	-0.57±0.18
	CBF	-19.05±3.21	-25.39±77.97	-22.04±4.35	-23.57±6.01
Motor cortex	BOLD	-0.60±0.20	-0.26±0.11	-0.24±0.08	-0.49±0.13
	CBF	-15.39±4.66	-14.04±3.78	-10.15±2.97	-15.63±3.19

Table 6.3: The maximum amplitude of the BOLD and CBF post-stimulus undershoot (in % change ± standard error) for visual and motor cortex ROI1 time courses averaged over all subjects.

(means of –22.57±2.74% and –13.80±1.81% for the visual and the motor cortex respectively) time courses. The magnitude of the undershoot did not change with the duration of the stimulation period (mean post-stimulus undershoot value of –0.56±0.08% and –18.16±2.34% for the BOLD and CBF data respectively, $F(3,21)<0.89, p>0.05$). These results indicate that the amplitude of the BOLD and CBF post-stimulus undershoot is relatively independent of the stimulation duration.

Post-stimulus undershoot duration: Table 6.4 summarizes the maximum duration of the post-stimulus undershoot in ROI1 time courses averages over all subjects.

For the BOLD data, the undershoot observed in the case of the visual cortex time course (mean of 42.88±3.55s) was significantly longer than in the case of the motor cortex (mean of 30.50±4.95s, $(F(1,7)=15.94, p<0.01)$. The undershoot duration did not vary significantly as the stimulation duration was increased (mean of 36.68±3.12s, $F(3,21)=0.21, p>0.05$).

ROI1 (8 subjects)		20s	40s	80s	120s
Visual cortex	BOLD	43.00±5.28	45.50±4.40	52.5±9.18	30.50±7.44
	CBF	42.50±7.33	39.00±7.84	54.00±12.02	33.00±12.82
Motor cortex	BOLD	33.50±6.23	25.00±9.58	29.50±12.80	34.00±11.46
	CBF	33.00±6.49	32.00±9.71	45.00±12.48	20.50±6.61

Table 6.4: The maximum duration of the BOLD and CBF post-stimulus undershoot (in seconds ± standard error) for visual and the motor cortex ROI1 time courses averaged across all subjects.

For the CBF data, the duration of the post-stimulation undershoot did not vary significantly with brain region ($F(1,7)=4.50$, $p>0.05$) or with stimulation duration (mean CBF undershoot was 37.44±3.48s, $F(3,21)=1.40$, $p>0.05$) . These results show that the duration of the post-stimulus undershoot is independent of the stimulation duration.

The present findings demonstrate that the duration and the maximum amplitude of the BOLD and CBF post-stimulus undershoot are independent of stimulation duration, suggesting that factors other than the elevated $CMRO_2$ levels are likely responsible for the undershooting of these functional signals.

6.2.2 ROI2: Analysis of functional data using microvascular ROI obtained by intersecting BOLD and CBF ROI volumes for each run

Sample BOLD and CBF time courses for the four stimulation conditions obtain from one subject's visual cortex ROI2 are shown in Figure 6.4 and 6.5 respectively. As mentioned earlier, the sensitivity of the statistical package to stimulation duration made it difficult to obtain ROI2 masks for all subjects for the 20s stimulation run. Thus, only four and six subjects were included in visual and motor analysis for the 20s stimulation condition and

an unequal Ns ANOVA was performed on the data. Clear BOLD and CBF time course undershooting was seen in most cases. The number of undershoots seen under each stimulation condition are summarized in Table 6.8.

Average positive response: Table 6.5 summarizes the average positive response of the ROI2 time courses averaged over all subjects.

The average positive response of the BOLD (mean of $1.76 \pm 0.06\%$) and the CBF (mean of 77.41 ± 4.215) time courses did not differ significantly with stimulation duration ($F(3,49)<2.73$, $p>0.05$), or between the brain regions ($F(1,49)<1.21$, $p>0.05$).

ROI2 (8 subjects)		20s	40s	80s	120s
Visual cortex	BOLD	$2.22 \pm 0.44^{\ddagger}$	1.86 ± 0.11	1.57 ± 0.09	1.79 ± 0.08
	CBF	$62.21 \pm 16.23^{\ddagger}$	67.96 ± 36.80	81.48 ± 19.82	96.25 ± 10.81
Motor cortex	BOLD	$1.72 \pm 0.16^{\dagger}$	1.69 ± 0.20	1.61 ± 0.17	1.89 ± 0.18
	CBF	$51.36 \pm 10.12^{\dagger}$	79.59 ± 9.06	78.03 ± 9.62	86.38 ± 5.93

Table 6.5:The maximum positive amplitude of the BOLD and CBF response (in % change $\pm$ standard error) for visual and motor cortex ROI2 time courses averaged over all eight subjects except where indicated ($^{\ddagger}n=4$, $^{\dagger}n=6$).

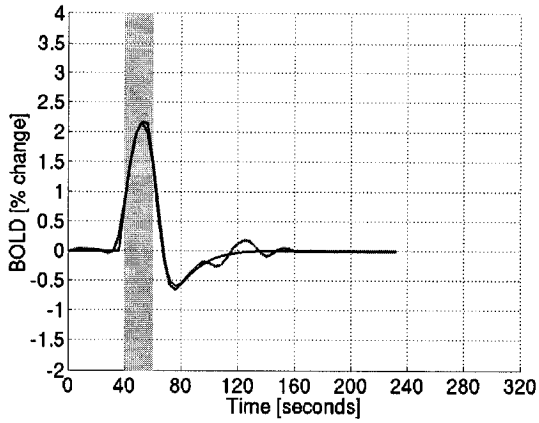

(A) 20s stimulation

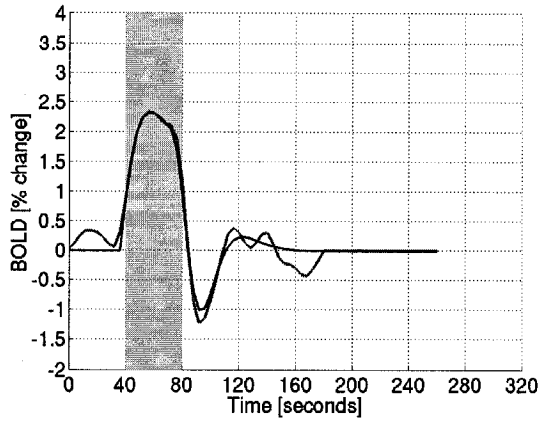

(B) 40s stimulation

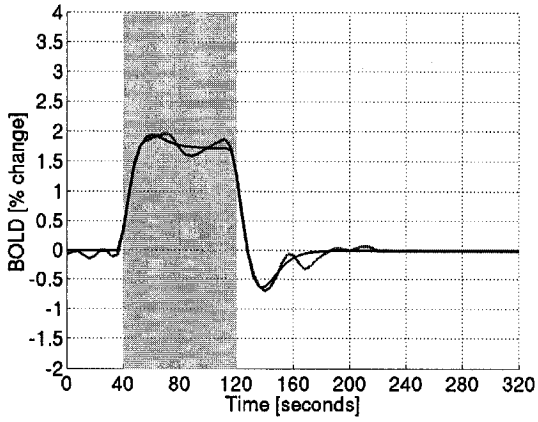

(C) 80s stimulation

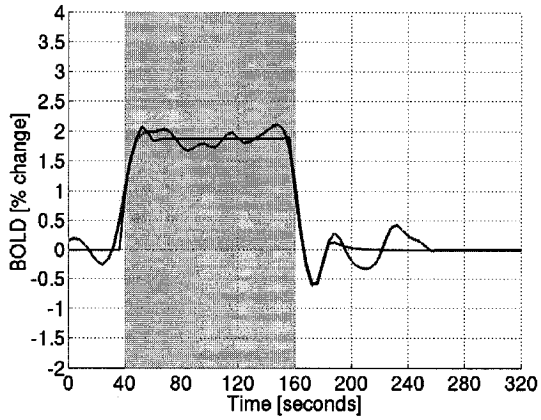

(D) 120s stimulation

Figure 6.4: BOLD time courses for the four stimulation conditions obtained from a sample subject's visual cortex ROI2 data. The shaded region signifies the stimulus ON period. The curve shown in red represents the time course from the temporally filtered (hanning window with FWHM of 20s) functional data while the black curve represents the HRF fitted to the data.

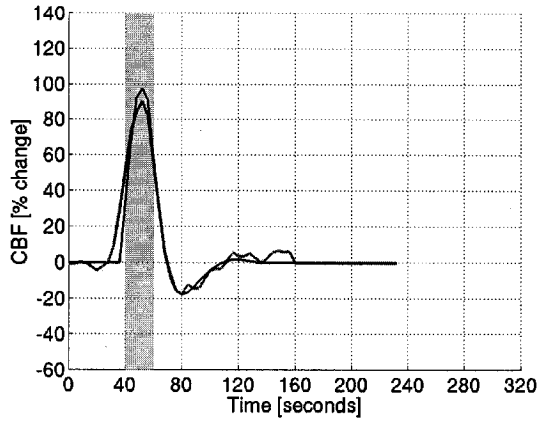

(A) 20s stimulation

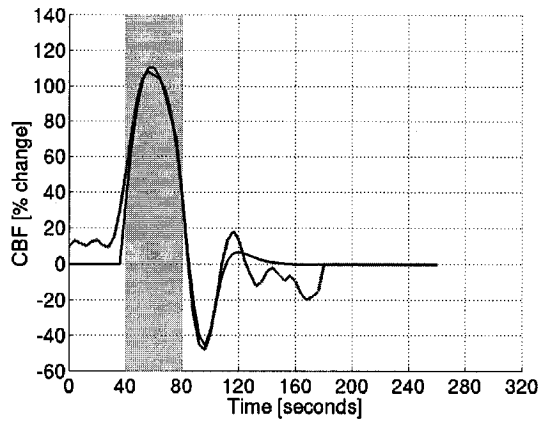

(B) 40s stimulation

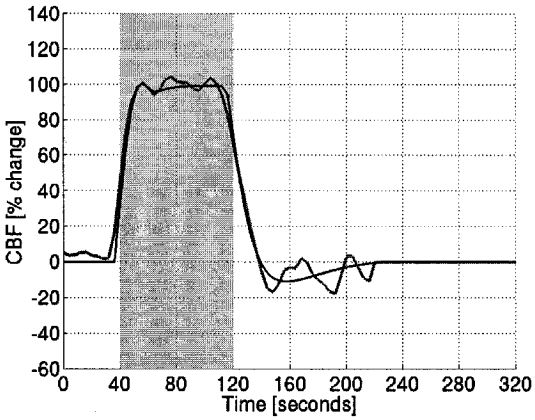

(C) 80s stimulation

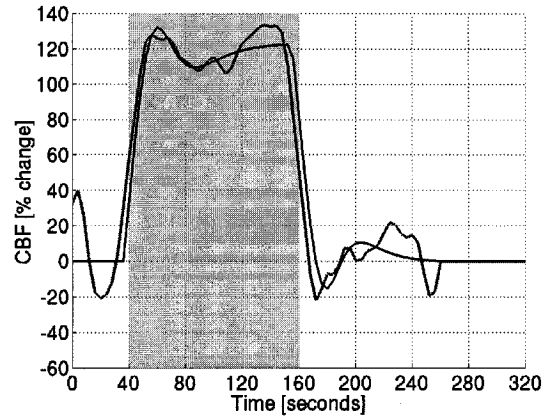

(D) 120s stimulation

Figure 6.5: CBF time courses for the four stimulation conditions obtained from a sample subject's visual cortex ROI2 data. The shaded region signifies the stimulus ON period. The curve shown in red represents the time course from the temporally filtered (hanning window with FWHM of 20s) functional data while the black curve represents the HRF fitted to the data.

Maximum undershoot amplitude: Table 6.6 summarizes the maximum undershoot amplitude for ROI2 time courses averaged over all subjects.

ROI2 (8 subjects)		20s	40s	80s	120s
Visual cortex	BOLD	-0.74 ± 0.14‡	-0.89 ± 0.10	-0.91 ± 0.14	-0.67 ± 0.14
	CBF	-16.24 ± 4.55‡	-25.88 ± 5.32	-21.32 ± 4.99	-24.63 ± 5.93
Motor cortex	BOLD	-0.48 ± 0.10†	-0.38 ± 0.09	-0.31 ± 0.07	-0.50 ± 0.13
	CBF	-7.20 ± 3.23†	-12.64 ± 3.95	-8.43 ± 2.89	-10.29 ± 2.96

Table 6.6: The maximum amplitude of the BOLD and CBF post-stimulus undershoot (in % change ± standard error) for visual and motor cortex ROI2 time courses averaged over all eight subjects except where indicated (‡n=4, †n=6).

The post-stimulus undershoot was significantly more pronounced (deeper) in the visual cortex than in the motor cortex for both BOLD (means of –0.82 ± 0.07% and –0.41 ± 0.05% in the visual and motor cortex respectively) and CBF (means of –23.09 ± 2.75% and –9.80 ± 1.62% in the visual and motor cortex respectively) time courses ($F(1,49)>11.45$, $p<0.005$). The duration of the stimulation period did not affect the amplitude of the BOLD (mean of –0.60 ± 0.05%) or CBF (mean of –16.10 ± 1.78%) undershoot ($F(3,49)<1.02$, $p>0.05$).

Post-stimulus undershoot duration: Table 6.7 summarizes the maximum duration of the post-stimulus undershoot in ROI2 time courses averages over all subjects.

ROI2 (8 subjects)		20s	40s	80s	120s
Visual cortex	BOLD	56.00±4.00	52.5±5.15	55.50±7.35	27.00±5.49
	CBF	36.00±13.85	44.5±7.25	51.00±11.40	24.00±6.41
Motor cortex	BOLD	46.67±3.68	37.5±7.71	38.00±10.82	30.5±7.71
	CBF	19.33±10.25	31.50±10.44	46.50±14.23	27.50±13.87

Table 6.7: The maximum duration of the BOLD and CBF post-stimulus undershoot (in seconds ± standard error) for visual and the motor cortex ROI2 time courses averaged across all subjects.

Statistical analysis revealed that for the BOLD data, the duration of the undershoot varied with stimulation duration ($F(3,49)=3.05$, $p<0.05$) but not with brain region ($F(1,49)=2.89$, $p>0.05$). Further analysis revealed that the undershoot was significantly longer during the 20s stimulation run than during the 120s stimulation run (means of 46.00±4.68s and 32.8±4.96s for the 20s and the 120s stimulation runs respectively). None of the other effects were significant (mean undershoot duration for the BOLD data was 41.34±2.92s).

For the CBF data, the duration of the post-stimulation undershoot did not vary significantly with either brain region ($F(1,49)=0.78$, $p>0.05$) or with stimulation duration ($F(3,49)=1.51$, $p>0.05$) (mean of 34.36±4.12s).

Similar to the ROI1 analysis, the present findings from ROI2 demonstrate that the duration and the maximum amplitude of the BOLD and CBF post-stimulus undershoot are relatively independent of stimulation duration.

ROI1 (8 subjects)		20s	40s	80s	120s
Visual cortex	BOLD	8	8	8	8
	CBF	8	7	8	7
Motor cortex	BOLD	7	4	5	7
	CBF	8	7	6	7
ROI2 (8 subjects)		**20s**	**40s**	**80s**	**120s**
Visual cortex	BOLD	4‡	8	8	7
	CBF	3‡	8	7	7
Motor cortex	BOLD	6†	8	7	7
	CBF	4†	8	5	6

Table 6.8: Summary of the number of post-stimulus undershoots seen in average time courses for each ROI and brain region (‡ of a total of 4 time courses, † of a total of 6 time courses).

Chapter 7

Discussion, Conclusion and Future Work

7.1 Experiment #1: Hypercapnia Study

The main finding of this experiment was that a clear post-stimulus undershoot was present in the BOLD time courses both with visual and motor stimulation as well as under hypercapnic perturbation. The corresponding CBF signal also showed pronounced post-stimulus undershooting.

7.1.1Effect of hypercapnia on cerebral hemodynamics

A consistent increase in the $ETCO_2$ values of ~6 and 15mm Hg were observed under the 5 and 10% hypercapnia perturbation conditions while the subjects maintained constant respiratory rates. These increases are similar to those observed in several other hypercapnia studies in humans [37, 102, 103], and confirm that the desired arterial CO_2 modulation was achieved.

The elevated $ETCO_2$ values under constant respiration rates signify increased $PaCO_2$ in the blood, which is known to cause global increases in CBF [80, 95, 96, 102]. Furthermore, since the $CMRO_2$ has been shown not to be effected by elevated CO_2 levels

in blood [96], hypercapnic perturbations result in an increase in the oxygen saturation of the venous circulation, or equivalently, a decrease in the concentration of deoxyhemoglobin via dilution. Thus, the occurrence of a post-stimulus undershoot in hypercapnic BOLD time courses strongly suggests that mechanisms other then the prolonged elevation in $CMRO_2$ levels are responsible for transient undershoot, at least under these specific circumstances.

Several recent studies have shown that the global BOLD signal increases mimic the CBF changes under hypercapnic perturbation [43, 104, 105]. In this study, post-stimulus CBF undershoots were seen in whole-brain and VC/MC hypercapnic time courses. Although it is not completely clear why the CBF signal would drop below baseline levels after the cessation of the hypercapnia, the undershoot seen in the BOLD signal is likely a direct result of this CBF undershoot.

7.1.2 Region of Interest Analysis

As discussed in chapter 4, ROI1 included all voxels that showed hypercapnia correlated signal changes throughout the cortex. Clear hypercapnia correlated increases and post-stimulus undershoots were observed in the BOLD and CBF signal time courses obtained from ROI1. These time courses represent global changes caused by the hypercapnia conditions.

ROI2 volumes were obtained by overlapping visual/motor stimulation t-maps from the visual/motor stimulation run with the hypercapnia masks from ROI1. A few subjects failed to show any overlap between the voxels that showed statistically significant stimulated activation and those that showed hypercapnia induced signal CBF

changes. Although this could be attributed to either inter-run head motion, low signal-to-noise in the CBF ASL data, or the noisy nature of hypercapnia data compared to the stimulation data, it is also noted that the CBF regulatory mechanism elicited by the administration of the CO_2 mixture is not identical to that underlying neuronal activation [106].

ROI1 responses are representative of an average of all cortical regions, where the homogeneity of cerebral hemodynamics amongst the different functional regions is not fully known, while ROI2 responses are specific to the well-characterized visual and motor regions alone. However, it is important to note that in this study, the time courses derived from both ROIs showed consistent BOLD and CBF undershoots during neuronal activation and hypercapnia.

7.1.3 Effect of elevated CO_2 on the BOLD and CBF response

As expected, the average positive BOLD response obtained from the 10% hypercapnic perturbation condition was higher than that of the 5% condition irrespective of the ROI used. Both whole brain analysis (using ROI1 volumes) and regional visual/motor analysis (using ROI2) revealed ~1.7% difference in response amplitude between the two conditions which is similar to that observed in previous studies by our group [37] and is in agreement with the average BOLD-$ETCO_2$ reactivity of 0.1-0.4% per mm Hg in gray matter reported in literature [107, 108].

While the average increase in the whole brain CBF response (using ROI1) was ~4%, which is well below the 2-11% flow increase per mm of Hg raise in $ETCO_2$ reported in other studies [37, 109, 110], more significant increases of ~25% were seen between 5% and 10% hypercapnic perturbation from ROI2 data. In the case of the whole

brain CBF data, although four of the eleven subjects showed ~25% increases between the two conditions, the inability to observe pronounced CBF increases between the two hypercapnia conditions may be due to the heterogeneity in the CBF response in different regions of the cortex, large CBF increases being offset by smaller CBF changes in physiologically distinct brain regions. The mismatch in the volumes used to calculate the CBF time courses under the two hypercapnic conditions could be another factor. Although the t-maps from the two runs were thresholded at the same statistical threshold, the ROI volumes for the 10% hypercapnia run were about four times the size of that of the 5% run.

Another important finding was that the duration and amplitude of the post-stimulation undershoot did not vary significantly with the hypercapnia level in either of the two ROIs. BOLD undershoots averaged out to ~-0.25% lasting ~45s while CBF undershoots were ~-13% lasting ~55s. (It should be noted that the values of the duration of the undershoot were estimated from fitting low-pass filtered time course data and as a result appear prolonged, as mentioned in Chapter 4.) In assuming the distensible venous vessels model, the BOLD undershoot dynamics depend on the elastic properties of the vessels as described by the Windkessel model [70]. In accordance with the above results, we speculate a maximal distention of the elastic venous vessels that is reached well before the 10% hypercapnia induces maximal CBF increases. Any additional increase in pressure on the venous vessel, due to additional elevation in CO_2 prompted CBF, does not elicit further ballooning. This concept of an upper limit to venous compliance, although not specifically addressed in either the balloon or the Windkessel models, has been suggested in other studies involving large hypercapnic perturbations [111].

The occurrence of CBF undershoots during hypercapnic stimulation in itself is rather puzzling. Although previous studies [7, 8] have reported a clear CBF undershoot during functional stimulation, reports of post-hypercapnia undershoots in the CBF signal are lacking in literature. CBF control during neuronal activity is regulated by a number of factors; temporal regulatory imbalances between the various modes of control are possibly responsible for the CBF undershoot. While direct neuronal control [112, 113, 114, 115], activation related neuron-to-astrocyte signaling [116], and signaling by metabolic indicators like adenosine/lactate [117] can be eliminated as mechanisms controlling CBF regulation during hypercapnic perturbation, changes in the concentration of bio-chemical indicators such as NO and CO_2 seem to be the only plausible driving force behind hypercapnic CBF regulation [95]. Since there is no evidence of post-hypercapnia undershooting in the $PaCO_2$ level in blood, a reduction in the CBF signal may be indicative of a "sling-shot" effect (slight vasoconstriction) occurring as the arterial and capillary vessels return to baseline diameters. A recent study provides evidence that CBF decreases at the capillary level are indeed possible [118]. Irrespective of the cause of the undershooting, the observation of clear CBF undershooting seems to favor the theory that the post-hypercapnia BOLD signal follows the CBF signal [8, 43, 76].

Results from this experiment, showing clear BOLD and CBF signal undershooting after the cessation of CO_2 induced hypercapnia, suggest that the ballooning in venous vessels and underlying CBF undershooting are both likely to be major contributors in BOLD post-stimulation undershooting in the absence of neuronal activation, given that elevated $CMRO_2$ levels can be ruled out as a possible source of the BOLD undershoot in the hypercapnia data. Although this conclusion is limited to hypercapnia, the evidence of

hypercapnia induced post-stimulus undershooting suggests a similar mechanism may be at play during activation induced CBF increases, thus implying that prolonged $CMRO_2$ is likely not the sole cause of the BOLD post-stimulus undershoot.

7.2 Experiment #2: Stimulation Duration Study

The main finding of this experiment was that post-stimulus undershooting, seen in both BOLD and CBF signal time courses, did not vary in amplitude or duration upon changing the duration of the stimulus 'ON' period.

7.2.1Region of Interest analysis

As explained in previous chapters, two ROI selection criteria were used to extract BOLD and CBF time courses. ROI1 comprised of activated voxels selected individually for each stimulation duration run. Although a high degree of inter-subject variability was observed in the sizes of the activation volumes, the volume of the ROI increased with total stimulation duration (i.e. ROI volumes for the 20s runs contained far fewer voxels than the 80s stimulation run). This discrepancy in selecting activated volumes can be attributed to the sensitivity of the *fMRIstat* [99] statistical package to the length of the activation paradigm; activated voxel corresponding to longer stimulation periods being easier to isolate.

As stated previously, a second ROI, obtained by selecting only the subset of voxels that showed both BOLD and CBF variation with stimulus during each stimulation run, was used to extract time courses from regions likely to be composed of microvasculature. The volumes obtained using this criterion were significantly smaller than those from ROI1, as expected.

7.2.2 Time courses analysis

Average Positive Response: As reported in Chapter 6, positive stimulus correlated BOLD increases of ~1.8% and CBF increases of ~75% were observed under visual and motor stimulation during the four stimulation conditions. As expected, these 3T BOLD values are significantly higher than those reported in previous 1.5 T fMRI studies from our lab (showing ~1% BOLD increase with similar motor and/or visual stimulation) [7, 37, 119].

Although the average positive response did not vary significantly with stimulation duration or between visual and motor regions, a few discrepancies were noticed. The average positive BOLD response to the 20s stimulation from ROI1 alone was significantly higher than the 40s and 80s stimulation runs, while the corresponding CBF response was slightly lower than that of the other three conditions. A possible explanation is that the shortest stimulation elicits a response similar to the initial overshoot seen in longer BOLD responses [7, 63, 64] while the inability to see a similar overshoot in CBF data might be attributed to the low CNR and temporal resolution of the CBF data.

Post-Stimulus Undershoot Dynamics: BOLD post-stimulus signal undershoots, of amplitude ~-0.75/-0.4% lasting ~42/31 seconds in the visual/motor cortices were seen. Correspondingly, CBF signal decreases of ~ -23/-12 % lasting ~42/30 seconds in the visual/motor cortices were observed. (It should be noted that the values of the duration of the undershoot were estimated from fitting low-pass filtered time course data and as a result appear prolonged, as mentioned in Chapter 4.) Overall, the amplitude and duration of the BOLD and CBF undershoot did not vary with stimulation duration. Assuming that the depletion of ions accumulates proportionally to the increase in stimulation period, these results suggest that sustained elevation in $CMRO_2$ levels (used to restore the ionic

gradients to their pre-activation levels) is evidently not the sole cause of the post-stimulus BOLD undershoot.

The post-stimulus undershoot was more pronounced and lasted longer in visual cortex BOLD and CBF data as compared with motor cortex data. This may be due to the fact that the 4Hz frequency of the visual stimulus used in this experiments produces larger BOLD and perfusion responses [7, 120], while no attempt has been made to match the finger tapping motor stimulus response to the visual stimulus response.

Clear CBF post-stimulus undershooting from both ROI1 and ROI2 time courses was seen under all four simulation conditions of ~-17 % lasting ~35seconds. Similar CBF signal undershoots have been reported in other fMRI studies [7, 8], implying possible arterial over-constriction after the end of the stimulation, as described in section *7.1.3*. Given that several mechanisms are concurrently responsible for vasodilation that accompanies neuronal activation, the undershooting in the CBF may be the result of a temporal regulatory imbalance between neurotransmitter signaling, NO/CO_2 vascular regulation and direct neuronal response that affect cerebral flow.

Our results provide strong evidence that the prolonged elevation in $CMRO_2$ levels alone can not explain the post-stimulation undershoot. The undershoot in the CBF likely plays an important role in the BOLD undershoot although the exact relationship between the two has yet to be established. The role of the ballooning was not directly tested; further venous CBV measurements would need to be performed to examine the extent to which the CBV time course affects the BOLD signal dynamics.

7.3 Conclusion and Future Work

In this thesis, two complementary BOLD and CBF fMRI experiments were conducted to assess the validity of the 'balloon model' and the 'elevated $CMRO_2$' theory as possible explanations for the occurrence of the post-stimulation undershoot transient seen in the BOLD fMRI signal. The results demonstrated without doubt, that elevated $CMRO_2$ after the cessation of the stimulation is not the only mechanism behind the BOLD undershoot; a more likely scenario being that venous ballooning combined with CBF undershoot results in a negative BOLD transient. Possible contribution from the post-stimulation elevation in $CMRO_2$ however, can not be ruled out.

Time courses showing BOLD and CBF post-hypercapnia undershooting, in the absence of $CMRO_2$ changes provide direct evidence that the CBF signal can be implicated in the BOLD post-hypercapnia. Further, the observation that some subjects did not show simultaneous CBF undershoots seems to suggest additional mechanisms, possibly venous ballooning as contributing factors to the overall BOLD undershoot.

Since no direct CBV measurements were made in both experiments, it was not possible to directly establish the extent to which the venous vessel volume contributed to the BOLD signal undershoot. Future work should include robust venous CBV measurements with a technique, such as VERVE [71], alongside BOLD and CBF measurements to directly determine the precise role of venous CBV changes in transient BOLD behavior.

Appendix A

Ethics approval for human studies

The human studies included in this thesis were approved by the Montreal Neurological Institute and Hospital Research Ethics Board. The following document is the confirmation of the approval.

References

[1] S. Ogawa, T. M. Lee, A. S. Nayak, P. Glynn. Oxygenation-sensitive contrast in magnetic resonance image of rodent brain at high magnetic fields. *Magn Reson Med*, 14: 68-76, 1990.

[2] S. Ogawa, D. W. Tank, R. Menon, J. M. Ellermann, S. G. Kim, H. Merkle, K. Ugurbil. Intrinsic signal changes accompanying sensory stimulation: functional brain mapping with magnetic resonance imaging. *Proc Natl Acad Sci USA*, 89(13):5951-5955, 1992.

[3] R. B. Buxton, E. C. Wong, L. R. Frank. Dynamics of blood flow and oxygenation changes during brain activation: the balloon model. *Magn Reson Med*, 39(6):855-864, 1998.

[4] R. B. Buxton, K. Uludaq, D. J. Dobowitz, T. T. Liu. Modeling the hemodynamic response to brain activation. *Neuroimage,* 23:S220-S233, 2004.

[5] J. Frahm, G. Kruger, K. D. Merboldt, A. Kleinschmidt. Dynamic uncoupling and recoupling of perfusion and oxidative metabolism during focal brain activation in man. *Magn Reson Med*, 35(2):143-148, 1996.

[6] G. Kruger, A. Kleinschmidt, J. Frahm. Dynamic MRI sensitized to cerebral blood oxygenation and flow during sustained activation of human visual cortex. *Magn Reson Med*, 35(6):797-800, 1996.

[7] R. D. Hoge, J. Atkinson, B. Gill, G. R. Crelier, S. Marrett, G. B. Pike. Stimulus-dependent BOLD and perfusion dynamics in human V1. *Neuroimage*, 9(6 pt 1):573-585, 1999.

[8] T. Obata, T. T. Liu, K. L. Miller, W. M. Luh, E. C. Wong, L. R. Frank, R. B. Buxton. Discrepancies between BOLD and flow dynamics in primary and supplementary motor areas: application of balloon model to the interpretation of BOLD transients. *Neuroimage,* 21(1):144-153, 2004.

[9]Source online: www.benet.org/teachers/meraci/Biology/FrBioReviews/ Nervous_System_Review/nervous_system_review.html.

[10] E. P. Widmaier, H. Raff, K. T. Strang. *Vander, Sherman & Luciano's Human Physiology: The mechanisms of Body Function.* McGraw Hill, Boston, MA, 2004.

[11] Source online: http://jnaccarato04.tripod.com/sitebuildercontent/sitebuilderpictures/ lwf0007.jpg.

[12] P. J. Magistretti, L. Pellerin, D. L. Rothman, R. G. Shulman. Energy on Demand, *Science*, 283(5401): 496-497, 1999.

[13] N. R. Sibson, A. Dhankhar, G. F. Mason, D. L. Rothman. Stoichiometric coupling of brain glucose metabolism and glutamatergic neuronal activity. *Proc Natl Acad Sci USA*, 95(1): 316-321, 1998.

[14] J. A. Sanders, W. W. Orrison. Functional magnetic resonance imaging. In W. W. Orrison, J. D. Lewine, J. A. Sanders, M. F. Hartshorne, editors, *Functional Brain Imaging,* pages 239-326. Mosby-Year Book, Inc. St.Louis, MO, 1995.

[15] A. C. Guyton, J. E. Hall. *Textbook of Medical Physiology.* W.B. Sansers Company, Philadelphia, 1996.

[16] T. Q. Duong, S. G. Kim. In vivo MR measurements of regional arterial and venous blood volume fractions in intact rat brain. *Magn Reson Med*, 43(3):393-402, 2000.

[17] Y. Zheng, D. Johnston, J. Berwick, D. Chen, S. Billings, J. Mayhem. A three-compartment model of the hemodynamic response and oxygen delivery to brain. *Neuroimage*, 28(4): 925-939, 2005.

[18] M. Raichle. The circulatory and metabolic correlates of functional activity. In M. Tomita, I. Kanno and E. Hamel, editors, *Brain Activation and CBF Control: Proceeding of the Satellite meeting on Brain Activation and Cerebral Blood Flow Control, held in Tokyo, Japan 5-8 June 2001,* pages 15-20. Elsevier Science, Amsterdam, The Netherlands, 2002.

[19] L. Sokoloff. Energy metabolism in neural tissues in vivo at rest and in functionally atlered states. In R.G. Shulman and D.L. Rothman, editors, *Brain energetics & neuronal*

activity applications to fMRI and medicine, pages 11-30. John Wiley & Sons Ltd., West Sussex, England, 2004.

[20] P. Fox, M. E. Raichle. Focal physiological uncoupling of cerebral blood flow and oxidative metabolism during somatosensory stimulation in human subjects. *Proc Natl Acad Sci USA,* 83(4): 1140-1144, 1986.

[21] R. B. Buxton. *Intorduction to Functional Magnetic Resonance Imaging,* pages 34-36, Cambridge University Press, 2002.

[22] B. J. Siesjo. *Brain Energy Metabolism.* Wiley, New York, 1978.

[23] C. Kennedy, M. H. Des Rosiers, O. Sakurada, M. Shinohara, M. Reivich, J. W. Jehle, L. Sokoloff. Metabolic mapping of the primary visual system of the monkey by means of the autoradiographic [14C] deoxyglucose technique. *Proc Natl Acad Sci USA,* 73(11):4230-4234, 1976.

[24] M. E. Phelps, J. C. Mazziotta. Positron emission tomography: human brain function and biochemistry. *Science,* 228(4701):799-809, 1985.

[25] L. Sokoloff. The relation between function and energy metabolism: its use in the localization of functional activity in the nervous system. *Neurosciences Research Progress bulletin,* 19:159-210, 1981.

[26] U. Gobel, B. Klein, H. Schrock, W. Kuschinsky. Lask of capillary recruitment in the brain of awake rats during hypercapnia. *J Cereb Blood Flow Metab,* 9(4):491-499, 1989.

[27] P. T. Fox, M. E. Raichle, M. A. Mintun , C. Dence. Nonoxidative glucose consumption during focal physiologic neural activity. *Science*, 241(4864):462-464, 1998.

[28] R. B. Buxton. Coupling between CBF and CMRO2 during neuronal activity. In M. Tomita, I,Kanno and E. Hamel, editors, *Brain Activation and CBF Control: Proceeding of the Satellite meeting on Brain Activation and Cerebral Blood Flow Control, held in Tokyo, Japan 5-8 June 2001,* pages 23-32. Elsevier Science, Amsterdam, The Netherlands, 2002.

[29] R. B. Buxton, L. R. Frank. A model for the coupling between cerebral blood flow and oxygen metabolism during neural stimulation. *J Cereb Blood Flow Metab,* 17(1):64-72, 1997.

[30] R.G. Shulman, F. Hyder, D.L.Rothman. Cerebral energetics and the glycogen shunt: neurochemical basis of functional imaging. *Proc Natl Acad Sci USA*, 98(11):6417-6422, 2001.

[31] J. Prichard, D. Rothman, E. Novotny, O. Petroff, T. Kuwabara, M. Avison, A. Howseman, C. Hanstock, R. Shulman. Lactate rise detected by 1H NMR in human visual cortex during physiologic stimulation. *Proc Natl Acad Sci USA*, 88(13):5829:5831, 1991.

[32] D. Sappey-Marinier , G. Calabrese , G. Fein , J. W. Hugg , C. Biggins , M. W. Weiner. Effect of photic stimulation on human visual cortex lactate and phosphates using 1H and 31P magnetic resonance spectroscopy. *J Cereb Blood Flow Metab*, 12(4):584-592, 1992.

[33] R. D. Hoge, J. Atkinson, B. Gill, G. R. Crelier, S. Marrett, and G. B. Pike. Linear coupling between cerebral blood flow and oxygen consumption in activated human cortex. *Proc Natl Acad Sci USA*, 96(16):9403-9408,1999.

[34] M. A. Mintun, B. N. Lundstrom, A. Z. Snyder, A. G. Vlassenko, G. L. Shulman, M. E. Raichle. Blood flow and oxygen delivery to human brain during functional activity: theoretical modeling and experimental data. *Proc Natl Acad Sci USA*, 98(12):6859-6864, 2001.

[35] W. J. Powers, I. B. Hirsch, P. E. Cryer. Effect of stepped hypoglycemia on regional cerebral blood flow response to physiological brain activation. *Am J Physiol,* 270 (2 pt 2):H554-H559, 1996.

[36] D. Attwell, C. Iadecola. The neural basis of functional brain imaging signals. *Trends Neurosci,* 25:621-625, 2002.

[37] B. Stefanovic, J. M. Warnking, K. M. Rylander, G. B. Pike. The effect of global cerebral vasodilation on focal activation hemodynamics. *Neuroimage,* 30(3):726-734, 2006.

[38] P. Jezzard, N. F. Ramsey. Functional MRI. In P. Tofts, editor, *Quantative MRI of the Brain: Measuring Changes Caused by Disease, pages 413-454.* Wiley, West Sussex, England, 2003.

[39] R. B. Buxton. *Introduction to Functional Magnetic Resonance Imaging*, pages 390-416. Cambridge University Press, 2002.

[40] R. B. Buxton. *Introduction to Functional Magnetic Resonance Imaging*, pages 352-387. Cambridge University Press, 2002.

[41] L. M. Parkes, J. A. Detre. ASL: Blood Perfusion Mesauremtnts Using Arterial Spin Labelling. In P. Tofts, editor, *Quantative MRI of the Brain: Measuring Changes Caused by Disease, pages 455-475.* Wiley, West Sussex, England, 2003.

[42] L. L. Ward. Basis of BOLD functional imaging contrast. In (HST. 583) Functional Magnetic Resonance Imaging: Data Acquisition and Analysis, *Lecture Notes*, 2004.

[43] R. D. Hoge, J. Atkinson, B. Gill, G. R. Crelier, S. Marrett, G. B. Pike. Investigation of BOLD signal dependence on cerebral blood flow and oxygen consumption: the deoxyhemoglobin dilution model. *Magn Reson Med*, 42(5): 849-863, 1999.

[44] G. S. Kim, K. Ugurbil. Comparison of blood oxygenation and cerebral blood flow effects in fMRI: estimation of relative oxygen consumption change. *Magn Reson Med.* 38(1):59-65, 1997.

[45] J. A. Detre, J. S. Leigh, D. S. Williams, A. P. Koretsky. Perfusion imaging. *Magn Reson Med*, 23(1): 37-45, 1992.

[46] D. S. Williams, J. A. Detre , J. S. Leigh, A. P. Koretsky . Magnetic resonance imaging of perfusion using spin inversion of arterial water. *Proc Natl Acad Sci USA*, 89 (1): 212-216, 1992.

[47] R. R. Edelman, B. Siewert, D. G. Darby, V. Thangaraj, A. C. Nobre, M. M. Mesulam, S. Warach. Qualitative mapping of cerebral blood flow and functional

localization with echo-planar MR imaging and signal targeting with alternating radio frequency. *Radiology*, 192(2):513-520, 1994.

[48] S. G. Kim. Quantification of relative cerebral blood flow change by flow-sensitive alternating inversion recovery (FAIR) technique: application to functional mapping. *Magn Reson Med*, 34(3): 293-301, 1995.

[49] E. C. Wong, R. B. Buxton, L. R. Frank. Implementation of quantitative perfusion imaging techniques for functional brain mapping using pulsed arterial spin labeling. *NMR Biomed*, 10(4-5):237-249, 1997.

[50] E.C. Wong, R.B. Buxton, L.R. Frank. Quantitative imaging of perfusion using a single subtraction (QUIPSS). *Neuroimage*, 3:S5, 1996.

[51] E. C. Wong, R. B. Buxton, L. R. Frank. Quantitative imaging of perfusion using a single subtraction (QUIPSS and QUIPSS II). *Magn Reson Med*, 39(5):702-708, 1998.

[52] J. Frahm, H. Bruhn, K. D. Merdoldt, W. Hanicke. Dynamic MR imaging of human brain oxygenation during rest and photonic stimulation. *J Magn Reson Imaging*, 2(5):501-505, 1992.

[53] R. S. Menon, S. Ogawa, D. W. Tank, K. Ugurbil. 4 Tesla gradient recalled echo characteristics of photon stimulation induced signal changes in human primary visual cortex. *Magn Reson Med*, 30(3):380-387, 1993.

[54] K. K. Kwong, J. W. Belliveau, D. A. Chesler, I. E. Goldberg, R. M. Weisskoff, B. P. Poncelet, D. N. Kennedy, B. E. Hoppel, M. S. Cohen, R. Turner, H. M. Cheng, T. J.

Brady, B. R. Rosen. Dynamic magnetic resonance imaging of human brain activity during primary sensory stimulation. *Proc Natl Acad Sci USA,* 89(12):5675-5679, 1992.

[55] S. A. Engel, D. E. Rumelhart, B. A. Wandell, A. T. Lee, G. H. Glover, E. J. Chichilnisky, M. N. Shadlen. FMRI of human visual cortex. *Nature,* 369(6481):525, 1994.

[56] A. Connelly, G. D. Jackson, R. S. Frackowiak, J. W. Belliveau, K.F. Vargha, D. G. Gadian. Functional mapping of activated human primary cortex with a clinical MR imaging system. *Radiology,* 188(1):125-130, 1993.

[57] R. T. Constable, G. McCarthy, T. Allison, A. W. Anderson, J. C. Gore. Functional brain imaging at 1.5T using conventional gradient echo MR imaging techniques. *Magn Reson Med,* 11(4):451-459, 1993.

[58] R. Turner, P. Jezard, H. Wen, K. K. Kwong, D. Le Bihan, T. Zeffiro, R. S. Balaban. Functional mapping of the human visual cortex at 4 and 1.5 Tesla using deoxygenation contrast EPI. *Magn Reson Med*, 29(2):277-279, 1993.

[59] T. Ernst, J. Hennig. Observation of a fast response in functional MR. *Magn Reson Med*, 32(1):146-149, 1994.

[60] R. S. Menon, S. Ogawa, X. Hu, J. P. Strupp, P. Anderson, K. Ugurbil. BOLD based functional MRI at 4 Tesla includes a capillary bed contribution: echo-planar imaging correlates with previous optical imaging using intrinsic signals. *Magn Reson Med,* 33(3):453-459, 1995.

[61] X. Hu, T.H. Le, K. Ugurbil. Evalution of the early response in fMRI in individual subjects using short stimulus duration. *Magn Reson Med,* 37(6):877-884, 1997.

[62] E. Yacoub, K. Ugurbil, N. Harel. The spatial dependence of the poststimulus undershoot as revealed by high-resolution BOLD- and CBF-weighted fMRI. *J Cereb Blood Flow Metab*, 26(5):634-644, 2006.

[63] G. Kruger, A. Kleinschmidt, J. Frahm. Stimulus dependence of oxygenation-sensitive MRI response to sustained visual activation. *NMR Biomed*, 11(2):75-79, 1998.

[64] G. Kruger, A. Kastrup, A. Takahashi, G. H. Glover. Simultaneous monitoring of dynamic changes in cerebral blood flow and oxygenation during sustained activation in the visual cortex. *Neuroreport,* 10(14):2939-2943, 1999.

[65] P. Frensson, G. Kruger, K. D. Merboldt, J. Frahm. The temporal characteristics of oxygen-sensitive MRI responses to visual activations in humans. *Magn Reson Med*, 39(6):912-919, 1998.

[66] J. Hennig, C. Janz, O. Speck, T. Ernst. Functional spectroscopy of brain activation following a single light pulse: examination of the mechanism of the fast initial response. *Int J Imaging Syst Technol,* 6:203-208, 1995.

[67] J. McIntosh, Y. Zhang, S. Kidambi, T. Harshbargar, G. Mason, G. M. Pohost, D. Twieg. Echo-time dependence of the functional MRI "fast response". *'Proc SMRM, 4th Scientific Meeting, New York 1996'.* vol. 1, page 284.

[68] D. Malonek, A. Grinvald. Interactions between electrical activity and cortical microcirculation revealed by imaging spectroscopy: implications for functional brain mapping. *Science,* 272(5261):551-554, 1996.

[69] J. B. Mandeville, J. J. A Marota, C. Ayata, M. A. Moskowitz, R. M. Weisskoff, B. R. Rosen. MRI measurement of the temporal evolution of relative $CMRO_2$ during rat forepaw stimulation. *Magn Reson Med*, 42(5):944-951, 1999.

[70] J. B. Mandeville, J. A. Marota, C. Ayata, G. Zaharchuk, M. A. Moskowitz, B. R. Rosen, R. M. Weisskoff. Evidence of a cerebrovascular postarteriole windkessel with delayed compliance. *J Cereb Blood Flow Metab*, 19(6):679-689, 1999.

[71] B. Stefanovic, G. B. Pike. Venous refocusing for volume estimation: VERVE functional magnetic resonance imaging. *Magn Reson Med*, 53(2):339-347, 2005.

[72] H. Lu, X. Golay, J. J. Pekar, P. C .M. van Zijl. Sustained poststimulus elevation in cerebral oxygen utilization after vascular recovery. *J Creb Blood Flow Metab*, 24(7):764-770, 2004.

[73] B. Conrad, J. Klingelhofer. Dynamics of regional cerebral blood flow for various visual stimuli. *Exp Brain Res.*, 77(2):437-441, 1989.

[74] K. Irikura, K. I. Maynard, M. A. Moskowitz. Sustained poststimulus elevation in cerebral oxygen utilization after vascular recovery induced by topical L-nitroarginine during vibrissal stimulation. *J Cereb Blood Flow Metab*, 14(1):45-48, 1994.

[75] T. L. Davis, R. M. Weisskoff, K. K. Kwong, R. Savoy, B. R. Rosen. Susceptibility contrast undershoot in not matched by inflow contrast undershoot. In '*Proc SMRM, 2nd Annual Meeting, San Francisco, 1994*', vol. 1, page 435.

[76] K. J. Friston, R. Mechelli, R. Turner, C. J. Price. Nonlinear Responses in fMRI: The balloon model, volterra kernels, and other hemodynamics. *Neuroimage,*12(4):466-477, 2000.

[77] M. L. Schroeter, T. Kupka, T. Milner, K. Uludag, D. Y. von Carmon. Investigating the post-stimulus undershoot of the BOLD signal- A simutalneous fMRI and FNIRS study. *Neuroimage,* 30(2):349-358, 2006.

[78] D. Attwell, S. B. Laughlin. An energy budget for signaling in the grey matter of the brain. *J Cereb Blood Flow Metab*, 21(10):1133-1145. 2001.

[79] S. Ogawa, R. S. Menon, D. W. Tank, S. G. Kim, H. Merkle, J. M. Ellerman, K. Ugurbil. Functional brain mapping by blood oxygenation level-dependent contrast magnetic resonance imaging: a comparison of the signal characteristics with a biophysical model. *Biophys J.* 64(3):803-812, 1993.

[80] R. L. Grubb, M. E. Raichle, O. J. Eichling, M. M. Ter-Pogossian. The effect of changes in $PaCO_2$ on cerebral blood volume, blood flow and mean vascular transit time. *Stroke,* 5:630-639, 1974.

[81] T. L. Davis, K. K. Kwong, R. M. Weisskoff, B. R. Rosen. Calibrated functional MRI: Mapping the dynamics of oxidative metabolism. *Proc Natl Acad Sci USA*, 95(4):1834-1839, 1998.

[82] J. L. Boxerman, P. A. Bandettini, K. K. Kwong, J. R. Baker, T. L. Davis, B. R. Rosen, R. M. Weisskoff. The intravascular contribution to fMRI signal change: Monte Carlo modeling and diffusion-weighted studies in vivo. *Magn Reson Med*, 34(1):4-10, 1995.

[83] J. L. Boxerman, L. M. Hamberg, B. R. Rosen, R. M. Weisskoff. MR contrast due to intravascular magnetic susceptibility perturbation. *Magn Reson Med*, 34(4):555-566, 1995.

[84] R. M. Weisskoff, C. S. Zuo, J. L. Boxerman, B. R. Rosen. Microscopic susceptibility variation and transverse relaxation: Theory and experiment. *Magn Reson Med*, 31(6):601-610, 1994.

[85] D. A. Yablonsky, E. M. Haake. Theory of NMR signal behavior in magnetically inhomogeneous tissue: the static dephasing regime. *Magn Reson Med*, 32(6):749-763, 1994.

[86] C. M. Feng, H. L. Liu, P. T. Fox, J. H. Gao. Comparison of experimental BOLD signal changes in event-related fMRI with the balloon model. *NMR Biomed*, 14(7-8):397-401, 2001.

[87] T. Mildner, D. G. Norris, C. Schwarzbauer, C. J. Wiggins. A qualitative test of the balloon model for BOLD-based MR signal changes at 3T. *Magn Reson Med*, 46(5):891-899, 2001.

[88] V. Toronov, S. Walker, R. Gupta, J. H. Choi, E. Grotton, D. Hueber, A. Webb. The role of changes in deoxyhemoglobin concentration and regional blood volume in the fMRI BOLD signal. *Neuroimage,* 19(4):1521-1531, 2003.

[89] H. Lu, X. Golay, J. J. Pekar, P. C. M. van Zijl. Functional magnetic resonance imaging based on changes in vascular space occupancy. *Magn Reson Med,* 50(2):263-274, 2003.

[90] J. B. Mandeville, J. J. A. Marota. Vascular filters of functional MRI: spatial localization using BLOD and CBV contrast. *Magn Reson Med*, 42(3):591-598, 1999.

[91] H. Lu, D. A. Soltysik, B. D. Ward, J. S. Hyde. Temporal evolution of the CBV fMRI signal to rat whisker stimulation of variable duration and intensity: A linearity analysis. *Neuroimage,* 26(2):432-440, 2005.

[92] Y. Yang, H. Gu, E. A. Stein. Simultaneous MRI acquisition of blood volume, blood flow and blood oxygenation information during brain activation. *Magn Reson Med,* 52(6):1407-1417, 2004.

[93] H. Lu, P. C. M. van Zijl. Experimental measurements of extravascular parenchymal BOLD effects and tissue oxygen extraction fraction using multi-echo VASO fMRI at 1.5T and 3T. *Magn Reson Med,* 53(4):808-816,2005.

[94] Source online: www.thefreedictionary.com/hypercapnia.

[95] C. Iadecola. Does nitric oxide mediate the increases in cerebral blood flow elicited by hypercapnia? *Proc Natl Acad Sci USA,* 89(9):3913-3916, 1992.

[96] S. S. Kety, C. F. Schmidt. The effects of altered arterial tensions of carbon dioxide and oxygen on cerebral blood flow and cerebral oxygen consumption of normal young men. *J Clin Invest,* 27(4):484-492, 1948.

[97] J. M. Warnking, G. B. Pike. Bandwidth-modulated adiabatic RF pulses for uniform selective saturation and inversion. *Magn Reson Med*, 52(5):1190-1199, 2004.

[98] R. J. Cox. AFNI: Software for analysis and visualization of functional magnetic resonance neuroimages. *Computers and Biomedical Research,* 29(3):162-173, 1996.

[99] K. Worsley, C. Liao, J. Aston, V. Petre, G. Duncan, F. Morales, A. Evens. A general statistical analysis for fMRI data. *Neuroimage,* 15(1):1-15, 2002.

[100] K. Ugurbil, G. Adriany, P. Anderson, W. Chen, R. Gruetter, X. Hu, H. Markle, D. S. Kim, S. G. Kim, J. Strupp, X. H. Zhu, S. Ogawa. Magnetic resonance studies of brain function and neurochemistry. *Annu Rev Biomed Eng,* 2:633-660, 2000.

[101] G. H. Glover. Deconvolution of impulse response in event-related BOLD fMRI. *Neuroimage,*9(4):416-429,1999.

[102] E. R. Cohen, K. Ugurbil, S. G. Kim. Effect of basal Conditions on the magnitude and dynamics of the blood oxygenation level-dependent fMRI response. *J Cereb Blood Flow Metab,* 22(9):1042-1053, 2002.

[103] M. Wieckowska. *Cerebral Blood Flow Measurements Using FMRI and PET: A Validation Study.* Master's thesis, McGill University, August 2002.

[104] E. R. Cohen, K. Ugurbil, S. G. Kim. Estimation of relative oxidative metabolic changes during motor activity using graded hypercapnic calibration at 4 Tesla. *Proc Intl Soc Magn Reson Med,* 9:1190, 2001.

[105] S. G. Kim, E. Rostrup, H. B. W. Larsson, S. Ogawa, O. B. Paulson. Determination of relative $CMRO_2$ from CBF and BOLD changes: significant increases of oxygen consumption rate during visual stimulation. *Magn Reson Med,* 41(6):1152-1161, 1999.

[106] R. P. White, C. Deane, P. Vallance, H. S. Markus. Nitric oxide synthase inhibition in humans reduces cerebral blood flow but not the hyperemic response to hypercapnia. *Stroke*, 29 (2):467-472, 1998.

[107] S. Posse, L. Kemna, B. Elghahwagi, S. Wiese, V. Kiselev. Effect of graded hypo-hypercapnia on fMRI contrast in visual cortex: quantification of T2* changes by multiecho EPI. *Magn Reson Med*, 46(2):264-271, 2001.

[108] E. Rostrup, I. Law, M. Blinkenberg, H. Larsson, A. Born, S. Holm, O. Paulson. Regional differences in CBF and BOLD responses to hypercapnia: a combined PET and fMRI study. *Neuroimage*, 11(2):87-97, 2000.

[109] L. Kwmna, S. Posse, L. Tellmann, T. Schmitz, H. Herzog. Independence of regional and global cerebral blood flow during visual stimulation: an O-15-butanol positron emission tomography study. *J Cereb Blood Flow Metab*, 21(6):664-670, 2001.

[110] S. Ramsay, K. Murphy, S. Shea, K. Friston, A. Lammertsma, J. clark, L. Adams, A. Guz, R. Frackowiak. Changes in global cerebral blood flow in humans: effect on regional cerebral blood flow during a neuronal activation task. *J Physiol*, 471:521-534, 1993.

[111] K. M. Sicard, T. Q. Duong. Effects of hypoxia, hyperoxia, and hypercapnia on baseline and stimulus-evoked BOLD, CBF and $CMRO_2$ in spontaneously breathing animals. *Neuroimage*, 25(3):850-858, 2005.

[112] J. F. Jr. Reinhard, J. E. Liebmann, A. J. Schlosberg, M. A. Moskowitz. Serotonin neurons project to small blood vessels in brain. *Science*, 206(4414):85-87, 1979.

[113] E. Vaucher, E. Hamel. Cholinergic basal forebrain neurons project to cortical microvessels in the rat: electron microscopic study with anterogradely transported Phaseolus vulgaris leucoagglutinin and choline acetyltransferase immunocytochemistry. *J Neurosci*, 15(11),7427-7441, 1995.

[114] L. S. Krimer, E. C. Muly, G. V. Williams, P. S. Goldman-Rakic. Dopaminergic regulation of cerebral cortical microcirculation. *Nat Neurosci*,1(4):286-289, 1998.

[115] C.D. Pascpalas, G.C. Papadopoulos. Ultrastructural evidence for combined action of noradrenaline and vasoactive intestinal polypeptide upon neurons, astrocytes, and blood vessels of rat cerebral cortex. *Brain Res Bull*, 45(3):247-259, 1998.

[116] M. Zonta, M. C. Augulo, S. Gobbo, B. Rosengarten, K. A. Hossmann, T. Pozzan, G. Carmignoto. Neuron-to-astrocyte signaling is central to the dynamic control of brain microcirculation. *Nat Neurosci,* 6(1):43-50, 2003.

[117] F. M. Farace, D. D. Heistad. Regulation of the cerebral circulation: role of endothelium and potassium channels. *Physiol Rev*, 78(1):53-97, 1998.

[118] E. Chaigneau, M. Oheim, E. Audinat, S. Charpak. Two-photon imaging of capillary blood flow in olfactory bulb glomeruli. *Proc Natl Acad Sci USA*, 100(22):13081-13086, 2003.

[119] B. Stefanovic, J. Warnking, G.B. Pike. Hemodynamic and metabolic response to neuronal inhibition. *Neuroimage,* 22(2):771-778, 2004.

[120] M. Vafaee, E. Mayer, S. Marrett, T. Paus, A.C. Evens, A. Gjedde. Frequency-dependent changes of cerebral metabolic rate of oxygen (CMRO2) in the human striate cortex. *Neuroimage*, 5, Abstr, S35, 1997.